[Short title + Author Name - P&H title] 17 (2024) 105940

Contents lists available at ScienceDirect

Arabian Journal of Chemistry

journal homepage: www.ksu.edu.sa

Electrochemical corrosion and product formation mechanism of M42 high-speed steel in NaH_2PO_4-Na_2SO_4 passivating electrolyte

Gang Cao [a], Huaichao Wu [a,*], Guangqin Wang [b], Long Nie [a], Kui Yuan [a], Bin Ji [a]

[a] School of Mechanical Engineering, Guizhou University, Guiyang 550025, China
[b] Guizhou Huangguoshu Jinye Technology Co., Ltd., Anshun 561000, China

ARTICLE INFO

Keywords:
High-speed steel
Electrochemical corrosion
Thermodynamic analysis
Characterization technique
Surface condition
Product formation

ABSTRACT

High-speed steel (HSS) rolls operate in harsh conditions, making them vulnerable to surface degradation. Material removal technology for repairing defective HSS roll surfaces is the most effective way to maintain their integrity and reduce production costs. Electrochemical corrosion machining, with its excellent machining capabilities, offers a promising method for repairing HSS roll surfaces. However, the outer working layer of these rolls is made of premium HSS containing passivating metallic elements, complicating its corrosion behavior, particularly in passivating electrolytes. To elucidate the corrosion behavior and uncover the underlying mechanisms of corrosion and product formation of HSS during electrochemical corrosion machining, this study investigates the electrochemical corrosion process and behavior of M42 HSS used in rolls within a NaH_2PO_4-Na_2SO_4 passivating electrolyte. Metallographic etching experiments indicated that M42 HSS comprises a tempered martensitic matrix along with M_2C and M_6C eutectic carbides. Characteristics of oxidative reactions for M42 HSS in the electrolyte were observed in cyclic voltammetry. By conducting anodic polarization tests, along with thermodynamic analysis and characterization techniques, the entire electrode system was thoroughly examined, including corrosion phenomena, varying processes, and underlying mechanisms of corrosion and product formation. Notably, this study is the first to construct a Pourbaix diagram for the M42 HSS-$H_2PO_4^-$-SO_4^{2-}–H_2O system. The thermodynamic analysis revealed that the applied potential variation significantly influences corrosion behavior of M42 HSS, confirming by the characterization results. The adsorption phenomenon on the cathodic surface requires a higher potential (such as 6 V) to occur. Electrochemical reactions primarily occur on the anodic surface, while the cathodic surface (or in the electrolyte) mainly engages in chemical reactions with no electronic participation. Furthermore, the electrochemical corrosion process of HSS is driven by one or more corrosion mechanisms, such as galvanic corrosion, pitting, or intergranular corrosion. Therefore, these findings from this study contribute to the development of repairing HSS roll surfaces based on electrochemical corrosion machining in future engineering applications.

1. Introduction

High-speed steel (HSS) rolls are known for their exceptional mechanical properties, including high hardness, strong quenching penetrability, and superior wear resistance, making them the primary tools for hot rolling operations in the modern steel rolling industry (Delaunois et al., 2022; Wang et al., 2023b). During hot rolling, these rolls are subjected to various degradation mechanisms (Liu et al., 2020b; Xu et al., 2021), such as thermal fatigue, oxidative wear, abrasive wear, and corrosion, all of which can compromise the rolls' surface integrity and lead to gradual deterioration and eventual failure. The condition of the roll surfaces plays a critical role in determining the quality of the final rolled products. However, premium HSS rolls inevitably develop surface defects over the course of their operational lifespan, particularly when subjected to harsh working conditions. To ensure the quality of the rolled products, rigorous inspection and repairing roll surfaces become necessary after a certain period of service (Subramanyam et al., 2022). When the dimensional accuracy of the roll deviates from the engineering requirements for the rolled products, replacing a new HSS roll is often required. However, in most cases, repairing HSS roll surfaces is a complex and challenging task.

Several technological approaches are currently being explored for

* Corresponding author.
E-mail address: hcwu@gzu.edu.cn (H. Wu).

https://doi.org/10.1016/j.arabjc.2024.105940
Received 17 March 2024; Accepted 24 July 2024
Available online 26 July 2024

repairing HSS roll surfaces. For instance, Liu et al. (Liu et al., 2020b) introduced a modified overlay technique using submerged arc welding for resurfacing HSS roll. However, their study does not evaluate the bonding strength between the coating and the matrix, nor does it test the technique under practical rolling conditions. Surface additive techniques like this face multiple challenges, including developing coating methodologies, calibrating equipment, optimizing processing parameters, and establishing reliable quality assessment methods. These challenges can lead to increased production costs for the steel rolling industry. In contrast, a more straightforward and effective approach involves material removal technology. Given that the outer working layer of HSS rolls comprises a typical tempered martensitic matrix with various carbides (such as MC, M_2C, and M_6C) (Delaunois et al., 2022; Liu et al., 2020b), the material composition significantly influences the material removal process. Electrochemical grinding (ECG) has emerged as a promising technology for machining hard-to-machine materials like HSS (Cao et al., 2022), addressing some of the limitations associated with traditional grinding methods (Yuan et al., 2020; Chaus et al., 2021). In ECG, the corrosion machining on the anodic surface, driven by electrochemical action, results in minimal processing stress, absence of surface burn defects, and reduced tool wear (Zhengyang and Yudi, 2021). The grinding function removes the corroded product layer from the anodic surface, yielding a high-quality finish. Therefore, electrochemical corrosion machining in ECG plays a critical role in the material removal process of HSS surfaces.

Understanding electrochemical corrosion process and behavior is the fundamental premise for achieving high-quality and efficient electrochemical corrosion machining. The understanding provides deeper insights into corrosion characteristics, guides the selection of processing parameters, and facilitates process improvements in electrochemical corrosion machining. To date, limited research on HSS in the field of electrochemical corrosion has primarily focused on optimizing corrosion processing parameters, selecting suitable electrolytes (or inhibitors), and refining the microstructure. For example, Xu et al. (Xu et al., 2011) used a back-propagation neural network to model the nonlinear relationship between the corrosion rate of high-vanadium HSS in H_3PO_4 and the electrolyte's concentration and corrosion time. Although this study does not delve deeply into the electrochemical corrosion behavior of this alloy in the given electrolyte, it will lay a foundation for optimizing corrosion processing parameters. In terms of electrolytes and inhibitors selection, Brett et al. (Brett and Melo, 1997) used various electrochemical testing methods to examine the effects of different anions on the electrochemical corrosion behavior of M2 HSS. They identified sulfate as the most aggressive anion towards HSS, providing a basis for further research on electrochemical corrosion in the presence of these anions. Kwok et al. (Kwok et al., 2007) found that refining the carbides in HSS and including noble metals like Cr, Mo, and W improved electrochemical corrosion performance in NaCl and $NaHCO_3$. This study offers valuable insights into modifying HSS microstructure and addressing corrosion in environments containing Cl^- and CO_3^{2-}. Shi et al. (Shi and Su, 2016) proposed that biopolymer derivatives could act as surface inhibitors for HSS, basing their analysis of electrochemical corrosion behavior solely on electrochemical impedance spectroscopy and dynamic potential polarization curves without examining the resulting corroded surface conditions. Furthermore, in our previous studies (Cao et al., 2022; Yuan et al., 2022), a passivating electrolyte containing $H_2PO_4^-$ and SO_4^{2-} showed excellent electrochemical corrosion performance for a specific roll grade of M42 HSS, yielding promising results in ECG. However, there is still a gap in understanding the electrochemical corrosion process, behavior, and associated mechanisms in the M42 HSS-$H_2PO_4^-$-SO_4^{2-}–H_2O system. Microstructural refinement in HSS is commonly achieved through alloying and heat treatment processes. Ripoll et al. (Ripoll et al., 2016) demonstrated that adding Nb to HSS hardfacing microstructure helped refine carbides at grain boundaries, enhancing matrix alloying, which improved the corroded product layer's quality in H_2SO_4. This research indicates that doping with certain alloying elements can enhance HSS quality. Additionally, Voglar et al. (Voglar et al., 2020) reported that modifying traditional heat treatment processes, including deep cryogenic treatment, contributed to microstructural refinement in HSS. Although this study does not thoroughly examine the corroded surface condition after different heat treatments, it suggests that these treatments could potentially improve corrosion resistance through microstructure modification.

The above literature provides some insights into the complex and multifaceted nature of HSS in the field of electrochemical corrosion. However, the reference value of these studies for the electrochemical corrosion process and behavior of HSS is constrained. Moreover, the underlying mechanisms of the corrosion behavior for HSS in specific electrolytes remain unclear. Therefore, based on our previous works (Cao et al., 2022; Yuan et al., 2022), this study aims to investigate the electrochemical corrosion of a specific roll grade of HSS in a specific electrolyte. The primary objectives are to gain a deeper understanding of the factors influencing the electrochemical corrosion process, to elucidate the corrosion relationship within the microstructure, and to uncover the mechanisms behind product formation involving passivating metallic elements.

In this study, metallographic etching experiments were first conducted to reveal the microstructure and composition of HSS in question. Subsequently, dynamic potential polarization tests were used to ascertain key factors influencing electrochemical corrosion, while cyclic voltammetry was used to capture the characteristics of electrochemical reactions. To further investigate the electrochemical corrosion process and behavior of HSS in the given electrolyte, anodic polarization tests were performed using dynamic potential polarization tests in different applied potential regions. Following anodic polarization tests, a suite of relevant characterization techniques – including scanning electron microscopy (SEM) with energy-dispersive X-ray spectroscopy (EDX), X-ray Diffraction (XRD), X-ray photoelectron spectroscopy (XPS), and inductively coupled plasma optical emission spectrometer (ICP-OES) – was used to examine product information across the entire electrode system, including the anode, cathode, electrolyte, and insoluble products. Moreover, a Pourbaix diagram for the system in question was constructed to provide a theoretical analysis for elucidating the observed electrochemical behavior. Finally, by combing experimental observations with the results from characterization analyses and thermodynamic studies, we revealed the underlying mechanisms that contribute to corrosion and product formation in HSS within the given electrolyte.

2. Material and methods

2.1. Materials

In this study, a certain roll grade of M42 HSS (W2Mo9Cr4VCo8) was investigated, with its chemical composition detailed in Table S1 (Supplement material). Following standard heat treatment processes of HSS rolls (Garza-Montes-de-Oca and Rainforth, 2009; Jovičević-Klug et al., 2021), the hardness reaches 66 HRC, conforming to the requirements for the working layer material of HSS rolls. The dimensions of the HSS samples used for metallographic etching and electrochemical testing were 10 mm × 10 mm × 3 mm. In the electrochemical testing experiments, one broad face of each HSS sample was exposed to create a working electrode (WE) with an area of 1 cm^2, while the remaining surfaces were sealed with epoxy resin and electrically connected to a piece of copper wire. Additionally, pure Pt samples measuring 20 mm × 20 mm × 0.1 mm were also prepared. The HSS and Pt samples were polished in a stepwise manner using a sequence of SiC sandpapers of varying grits, followed by a final polish with an alumina-based polishing agent with a particle size of 500 nm. The polished samples were then degreased and cleaned with petroleum ether and anhydrous ethanol in an ultrasonic cleaner, and subsequently dried, sealed, and stored for

latter experimental use. As reported by our previous studies (Cao et al., 2022; Yuan et al., 2022), a passivating electrolyte suitable for ECG of M42 HSS was developed. The electrolyte (189.82 g·L^{-1} $NaH_2PO_4 \cdot 2H_2O$ + 40.12 g·L^{-1} Na_2SO_4) was formulated with analytical-grade reagents (Kermel, China) and deionized water (18.25 Ω·cm), with its chemical composition provided in Table S2 (Supplement material). Notably, for clarity in the following text, this electrolyte is referred to as the H_2PO4^--SO_4^{2-} passivating electrolyte.

2.2. Metallographic etching

The M42 HSS sample underwent chemical etching for 6 s using a 4 vol% nitric acid-alcohol solution at 25 °C. Following etching, the alloy's microstructure was examined using a metallographic microscope, with additional insights provided by electron microscopy. Further, the EDX technique was used to characterize the composition of the alloy in detail.

2.3. Electrochemical testing experiments

The electrochemical testing system consisted of an electrochemical workstation (DH7001, China), a computer, a traditional three-electrode configuration, and a temperature control device, as shown in Fig. 1. The M42 HSS sample was used as WE, while the reference electrode (RE) was an Ag/AgCl electrode with 3.5 mol·L^{-1} KCl (E_0 = +0.201 V), and the counter electrode (CE) was a Pt sheet. A temperature control device ensured a stable testing environment (±0.5 °C), with the electrolyte remaining static and exposed to air throughout the entire testing procedure. Unless otherwise noted, all testing potentials were referenced to RE.

To evaluated the effects of immersion time and temperature on electrochemical corrosion, dynamic potential polarization tests were conducted across a range of −2 to 3 V for immersion time and from the corrosion potential (E_{COR}) up to 3 V for temperature variations, at a scan rate of 2 mV·s^{-1} (Zeng et al., 2020). In cyclic voltammetry, the applied potential was scanned in the positive direction form the potential E_{COR} to the pitting potential (E_{TR}), then reversed to the original potential E_{COR} at a rate of 20 mV·s^{-1} (Liu et al., 2020a). To investigate the effect of applied potential on the electrochemical corrosion process, anodic polarization was performed in four defined potential regions using dynamic potential polarization tests at a scan rate of 2 mV·s^{-1}. These applied potential regions were classified as the active dissolution region (E_{COR}~E_{AP} (active potential)), the end of transition (E_{COR}~E_{FL} (Fred potential)), the end of passivation (E_{COR}~E_{TR}), and the end of transpassive dissolution (E_{COR}~E_{END} (ending potential)). For clarity in the following text, once the anode undergoes polarization in these applied regions, they are labeled as "after active dissolution," "after the end of transition," "after the end of passivation," and "after transpassive dissolution," respectively. Moreover, the constant potential tests were used to examine products on the cathodic surface, applying a constant potential of 6 V for 15 min. To ensure a clean testing surface, a potential of −1.5 V was applied for 2 min before these electrochemical tests to remove any oxide film that might have formed on the M42 HSS sample.

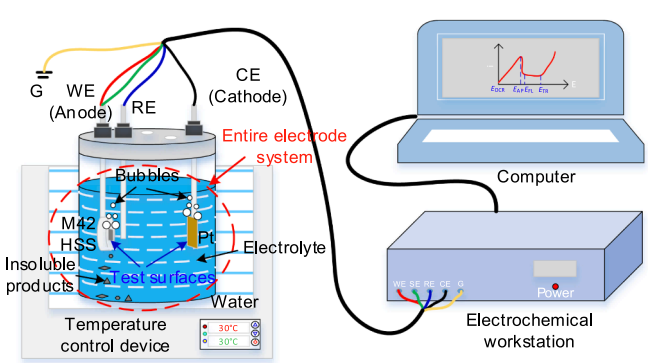

Fig. 1. Schematic of the electrochemical testing system.

2.4. Measurement and characterization methods

The thickness of the corroded product layer was measured using a coating thickness gauge (LS225, China). The pH value of the electrolyte was determined by a pH meter (LC-PHB-1A, China), while its conductivity was assessed with a conductivity meter (DDJB-350, China). Metallographic analysis of M42 HSS samples after chemical etching was conducted using a metallographic microscope (ICX41M, China). Characterization of the microstructure and composition of M42 HSS samples (both before and after corrosion), along with Pt samples, was performed using an electron microscopy (SEM (Tescan Mira 4, Czech) with EDX (Xplore 30, UK)). Corroded products on M42 HSS samples was conducted through grazing incidence XRD (SmartLab 9 kW, Japan). The component of insoluble products in the electrolyte was characterized using XRD (Bruker D8 Advance, Germany). The composition, chemical states, and possible substances on the electrode surfaces were analyzed by XPS (Thermo Scientific ESCALAB Xi+, USA). XPS peak fitting was performed using the Advantage 5.948 software, with calibration based on the C 1 s binding energy at 284.8 eV for all spectra. During the XPS peak fitting, peaks with spin–orbit splitting were adjusted according to specific intensity ratios and identical full width at half maximum (FWHM) (Klocke et al., 2018; Liu et al., 2020a). Additionally, the composition of M42 HSS samples and the used electrolyte were analyzed through ICP-OES (Agilent 5110, USA).

2.5. Thermodynamic calculation

In materials science, particularly in the context of hydrochemistry, the Pourbaix diagram (also known as the *E*-pH diagram) is a critical tool for analyzing thermodynamic stability (Banu et al., 2019; Wang et al., 2022a,b). Although the Pourbaix diagram has limitations in providing insights into corrosion kinetics (Ma et al., 2024), its importance for thermodynamic analysis is widely acknowledged. The Pourbaix diagram not only indicates the likelihood of reactions occurring in specific aqueous environments for metals and their alloys, but also helps determine the pathways of chemical reactions and identify the prevalent dominant species (Zhou et al., 2021; Wang et al., 2022a,b). The Pourbaix diagram is invaluable for discussing and analyzing possible reactions, stability regions of dominant species, and variations during the electrochemical corrosion process for passivating metallic elements (such as Fe and Cr). Therefore, in this study, constructing a Pourbaix diagram for M42 HSS in H_2PO4^--SO_4^{2-} passivating electrolyte is essential. Notably, in the M42 HSS-$H_2PO_4^-$-SO_4^{2-}–H_2O system, a general form of reactions is as follows (Zhou et al., 2021; Wang et al., 2022a,b):

$$aA + bH^+ + ne^- = cB + dH_2O \quad (1)$$

where *a*, *b*, *c*, and *d* denote stoichiometric coefficients for reactant A, H^+, product B, and H_2O, respectively; *n* is the number of electrons involved in the reaction. If the formation of water is disregarded, the equilibrium potential for Reaction (1) under isothermal and isobaric conditions can be derived from the following equation (Benabdellah et al., 2011).

$$E = -\frac{\Delta G^0(T)}{nF} - \frac{2.303bRT}{nF}\mathrm{pH} - \frac{2.303RT}{nF}\lg\frac{[B]^c}{[A]^a} \quad (2)$$

where *E* denotes the equilibrium potential (V); *T* denotes the temperature (K); $\Delta G^0(T)$ is the Gibbs free energy of the Reaction (1) (kJ·mol^{-1}), derived by extrapolation from the standard state Gibbs free energy $\Delta G^0(298.15)$; *R* is the ideal gas constant (8.31 J·(K·mol)$^{-1}$); pH denotes the acidity and alkalinity of the aqueous solution (pH = lg[H^+], [H^+] is the activity of H^+); *F* is the Faraday constant (96485.33 C·mol^{-1}); [B] is the activity of product B (mol·L^{-1}); and [A] is the activity of reactant A (mol·L^{-1}), respectively.

The Pourbaix diagram derived from Reaction (1) presents four distinct types: (i) Reactions that involve only H^+ without electron transfer (where $b \neq 0$, $n = 0$), appearing as vertical lines; (ii) Reactions that involve only electron transfer without H^+ activity (where $b = 0$, $n \neq 0$), appearing as a horizontal line; (iii) Reactions that involve both electrons and H^+ activity (where $b \neq 0$, $n \neq 0$), appearing as diagonal lines; and (iv) Reactions that are unaffected by both potential and H^+ activity, which cannot be appeared within the Pourbaix diagram.

Furthermore, in systems characterized by temperatures exceeding room temperature under atmospheric pressure conditions ($T \geq 298.15$ K), assuming negligible pressure sensitivity, the determination of $\Delta G^0(T)$ is calculated using the Criss-Cobble's method (Criss and Cobble, 1964; Zhao et al., 2019):

$$\Delta G^0(T) = \Delta G^0(298.15) - (T - 298.15)\Delta S^0(T) + \int_{298.15}^{T} \Delta C_p^0(T)\mathrm{d}T - T \times \int_{298.15}^{T} \frac{\Delta C_p^0(T)}{T}\mathrm{d}T \tag{3}$$

where $\Delta S^0(T)$ denotes the entropy at temperature T (J·(K·mol)$^{-1}$), and $\Delta C_p{}^0(T)$ denotes the average heat capacity at temperature T (J·(K·mol)$^{-1}$). At a given temperature T, $\Delta S^0(T)$ can be calculated as $\Delta S^0(T) = f_T + h_T \cdot \Delta S^0(298.15)$. The coefficients f_T and h_T vary with T, but they show minimal variations in the range from 25 to 60 °C (Criss and Cobble, 1964; Yang et al., 2016; Zhao et al., 2019), allowing for an approximation of $\Delta S^0(T) \approx \Delta S^0(298.15)$. However, temperature-induced variations are applied to correct the changes for $\Delta C_p{}^0(T)$ (Roy et al., 2012):

$$\Delta Cp^0(T) = k_1 + k_2 \cdot 10^{-3}T + k_3 \cdot 10^5 T^{-2} \tag{4}$$

where k_1, k_2, and k_3 are coefficients. Thus, the equilibrium potential of Reaction (1) can be ascertained from Equations (2) ~ (4).

3. Results and discussion

3.1. Microstructure and composition of M42 HSS

In the field of electrochemical corrosion, anodic metals or their alloy materials undergo degradation by electrocatalysis, resulting in the formation of ionic states or other corroded products. The microstructural characteristics of the material are crucial in determining electrochemical corrosion behavior and process (Klocke et al., 2018). Fig. 2(a)–(c) show the microstructure of M42 HSS after heat treatment. M42 HSS comprises a grey needle-like tempered martensite matrix and various white eutectic carbides. Unfortunately, metallographic microscopy makes it difficult to identify grain boundaries. Larger carbides tend to cluster near these boundaries, while smaller spherical carbides (≤0.6 μm) are evenly dispersed throughout the matrix. The outstanding mechanical properties of HSS stem from these carbides and the matrix's solid-solution strengthening phase (Jiao et al., 2022a). Notably, the variation in precipitate size of M42 HSS is significant, with the larger precipitates in the images measuring approximately 10 to 15 μm. The size of these precipitates could substantially affect the corrosion behavior of the metal. Additionally, residual shrinkage pores near the grain boundaries are observed, likely resulting from cooling processes during metallurgical formation and heat treatment. Fig. 2(d)–(f) present the microstructural composition of M42 HSS. The eutectic carbides primarily consist of M_2C (Mo-rich) and M_6C (Fe- and Mo-rich) carbides, where "M" represents alloying elements such as Fe, Mo, and W, as similarly reported by Jiao et al. (Jiao et al., 2022a,b). However, in contrast to their observations on the microstructure of as-cast M42 HSS, the M_6C carbides no longer exhibit a fishbone-like structure after heat treatment but appear as fine spherical particles. M_2C carbides display varied morphologies, including lamellar, blocky, and rod-like shapes. The M_2C eutectic carbides are metastable, making them susceptible to separation and spheroidization during the heating process (Garza-Montes-de-Oca and Rainforth, 2009; Chaus et al., 2019). Hence, the heat treatment processing is effective in refining and modifying the microstructure of HSS. However, addressing issues like the segregation of alloying elements during solidification, which may lead to the formation of large blocky carbides, requires further investigation. This should not only focus on the heat treatment processes but also consider approaches like alloy element doping or surface nitriding treatments, topics that beyond the scope of the present study.

Furthermore, the EDX results indicate the presence of noble elements such as Co, Cr, W, and V, alongside the primary components of Fe and Mo, in both the carbides and the matrix of M42 HSS. Table 1 provides

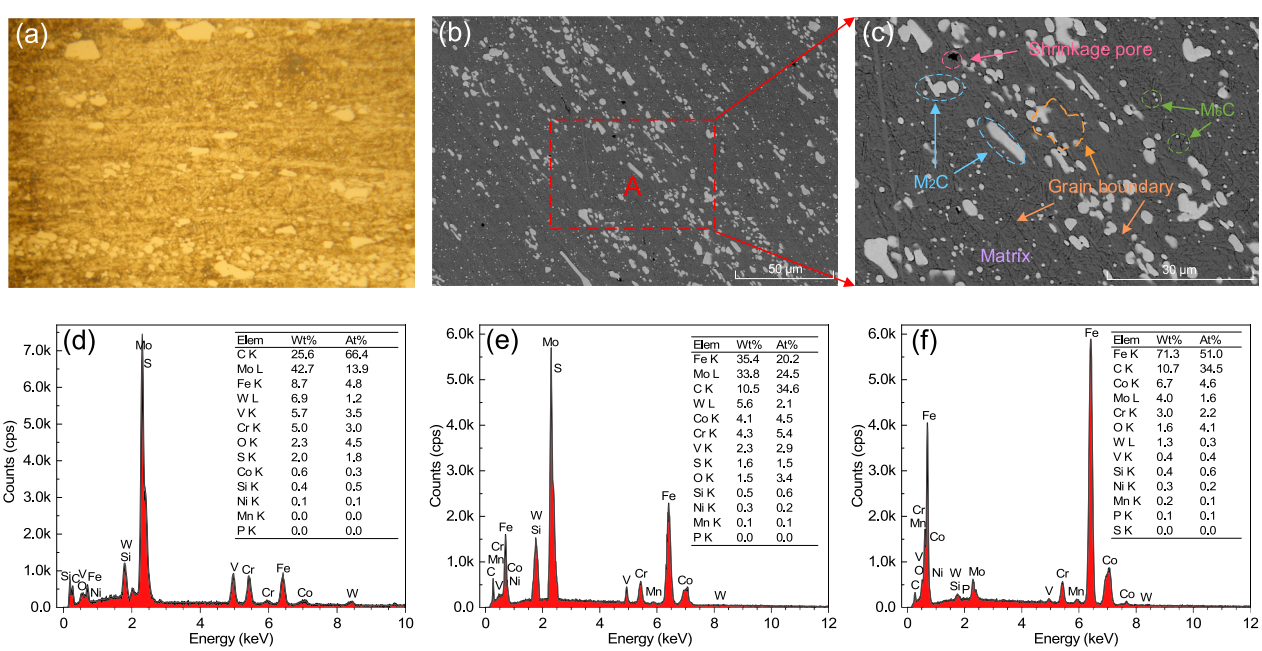

Fig. 2. Microstructure and composition of M42 HSS: (a) metallographic image, (b) SEM image, (c) local enlargement of area A, (d) EDX spectrum of M_2C, (e) EDX spectrum of M_6C, and (f) EDX spectrum of shrinkage pores and matrix.

Table 1
Electrode reactions and standard electrode potentials of metallic elements in M42 HSS.

Electrode reactions	Standard electrode potentials (V, vs. SHE)
$W \rightarrow W^{3+} + 3e^-$	+0.101
$Mo \rightarrow Mo^{3+} + 3e^-$	−0.130
$Ni \rightarrow Ni^{2+} + 2e^-$	−0.236
$Co \rightarrow Co^{2+} + 2e^-$	−0.282
$Fe \rightarrow Fe^{2+} + 2e^-$	−0.440
$Cr \rightarrow Cr^{2+} + 2e^-$	−0.890
$V \rightarrow V^{2+} + 2e^-$	−1.125
$Mn \rightarrow Mn^{2+} + 2e^-$	−1.182

the standard electrode potentials of these elements (Bratsch, 1989). The standard electrode potentials relative to the standard hydrogen electrode (SHE) vary significantly among these elements. For example, the electrode potential for Mn is −1.182 V, whereas that for W is 0.101 V. According to the electrochemical corrosion theory (Ghali, 2010), a more negative electrode potential indicates a greater propensity for electrochemical corrosion, and vice versa. Thus, the variability in electrode potentials among the metallic elements in M42 HSS can lead to selective corrosion during the electrochemical corrosion process.

3.2. Determination of experimental parameters

Some literature (Liu et al., 2020a; Zhou et al., 2021) suggests that, before electrochemical corrosion testing, metals and their alloys are generally immersed in the electrolyte for a predetermined duration to stabilize the surface. Fig. 3(a) presents the polarization curves of M42 HSS in the H_2PO4^--SO_4^{2-} passivating electrolyte at 25 °C after different immersion times. The results highlight the significant influence of immersion time on the electrochemical corrosion behavior of M42 HSS. Compared to the non-immersed condition, after 0.5 h of immersion, alongside a comparable active dissolution process, the potentials for E_{AP} and E_{FL} shift slightly to the left, and the current density exhibits a gradual increase in the passive region. However, with immersion times exceeding two hours, the potential ranges of the active dissolution and passive regions become narrower, resulting in the emergence of two distinct passive regions. This observation may be attributed to the formation of corroded product film during prolonged immersion, which stabilizes the surface and retards further dissolution, consequently reducing the current density. As the applied potential increases, the alloy's surface condition becomes increasingly complex, potentially involving rupture, dissolution, and formation of corroded products.

The electrolyte temperature also plays a critical role in electrochemical corrosion behavior of metals and their alloys. Fig. 3(b) depicts the polarization curves of M42 HSS in the H_2PO4^--SO_4^{2-} passivating electrolyte at different temperatures. As the temperature increases, the potentials for E_{AP} and E_{FL} shift rightward, with a corresponding increase in current density, suggesting that higher temperature facilitates the dissolution of the alloy. However, the potential E_{TR} remains unaffected by temperature, though there is a narrowing of the potential range within the passive region, accompanied by a tendency toward higher relative stable current density. Moreover, compared to temperatures below 30 °C, excessively high electrolyte temperatures lead to a significant increase in current density, particularly in the transpassive dissolution region. This behavior approximately aligns with Ohm's law, demonstrating a linear relationship between applied potential and current density (Wang et al., 2024). Higher electrolyte temperatures accelerate the exchange rate of active ions (Wang et al., 2019) and lead to a linear increase in electrolyte conductivity (Fig. 3(c)), thereby enhancing the current density. Therefore, the H_2PO4^--SO_4^{2-} passivating electrolyte at 30 °C is suitable for the electrochemical corrosion process of M42 HSS. However, prolonged immersion of the alloy in the electrolyte should be avoided to prevent any detrimental effects on subsequent electrochemical corrosion testing.

3.3. Reaction characteristics

Cyclic voltammetry is a crucial electrochemical testing technique

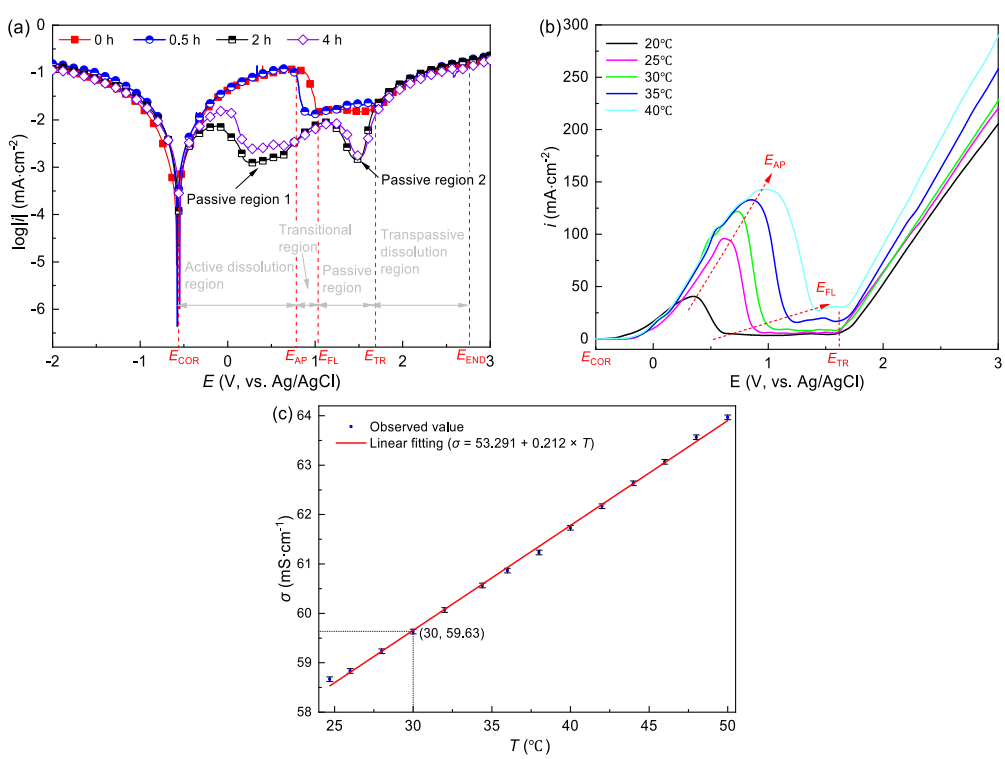

Fig. 3. (a) Polarization curves of M42 HSS in the H_2PO4^--SO_4^{2-} passivating electrolyte after different immersion times; (b) Polarization curves of the alloy in the same electrolyte at different temperatures; (c) Variation in the conductivity of the passivating electrolyte with the temperature.

that helps elucidate the chemical reaction state, adsorption process, and electron transfer mechanisms on the surface of a given electrode (Liu et al., 2020a; Munawar et al., 2023). To better understand the reaction characteristics and behavior of the electrochemical corrosion process for M42 HSS in the $H_2PO_4^-$-SO_4^{2-} passivating electrolyte, cyclic voltammetry tests were performed, with results depicted in Fig. 4. Starting from the potential E_{COR}, the first subtle oxidation peak, labeled A1, appears during the forward scan (Fig. 4(b)). The relationship between RE and SHE is described by Equation (5) (Macdonald et al., 1979):

$$E_{\text{vs. SHE}} = E_{\text{vs. Ag/AgCl}} + E_0 + D(T - T_0) \tag{5}$$

where E_0 represents the standard potential of RE (V), while the term $D(T-T_0)$ is considered negligible. Thus, at the peak A1 ($E_{\text{vs. SHE}} \approx -0.219$ V), all metallic elements except W and Mo undergo oxidation, as shown in Table 1. As the applied potential increases, the current density displays an approximately linear increase (Fig. 4(a)). Upon reaching the potential E_{AP}, a second oxidation peak, A2, emerges. This can be primarily attributed to the passivation of the alloy surface, which limits the migration of active ions within the electrolyte (Zeng et al., 2020). As a result, a significant decrease in current density occurs before reaching the potential E_{FL}. Although the minimum current density in the passive region is 75 mA·cm^{-2}, this suggests that the corrosion product film might have conductive properties or contain defects (such as porosity), allowing for continued electrochemical corrosion, ultimately leading to the appearance of the third oxidation peak, A3. During the reverse scan, no reduction peaks are observed, and the current density in the passive region remains nearly zero, indicating that the corroded products on the alloy surface are not reducible to a lower valence state. However, as the applied potential enters the active dissolution region, an oxidation peak, C2, becomes apparent, possibly due to the breakdown response of the corroded product film at certain weak points on the alloy surface (Barchiche et al., 2010). Scanning the applied potential to approximately −0.41 V reveals a subtle oxidation peak, C3, which appears to correlate with the initial oxidation behavior observed at peak A1. Furthermore, the effects of surface passivation on oxidation become apparent with repeated cycles. Unlike the first cycle, the current density gradually decreases with each subsequent cycle, suggesting that the corroded product film on the alloy surface does not fully prevent electrochemical corrosion. Nevertheless, near peak C1, a disruption in current density is observed, likely caused by the combined effects of the breakdown and passivation, with inherent defects in the corroded product film. In summary, the electrochemical corrosion process for M42 HSS in the $H_2PO_4^-$-SO_4^{2-} passivating electrolyte is primarily characterized by oxidative reactions during forward and reverse scans. The reverse scan helps determine if the corroded product film on the alloy surface contains defects or exhibits reduction characteristics.

3.4. Electrochemical corrosion process under anodic polarization

The multi-element HSS alloys present significant challenges in understanding electrochemical corrosion, particularly in terms of passivating metallic elements within specific media environments. To thoroughly gain insights into the electrochemical corrosion process and behavior for M42 HSS in the H_2PO4^--SO_4^{2-} passivating electrolyte, anodic polarization tests were performed using a forward linear scan of applied potential (i.e., dynamic potential polarization) in different applied potential regions, based on the results of cyclic voltammetry. The applied potential regions, as outlined in Section 2.3, included key potentials such as E_{AP}, E_{FL}, and E_{TR} that derived from Fig. 3(a). The potential E_{END} was set at 3 V. Alongside polarization tests, a suite of relevant characterization techniques was used to examine product information across the entire electrode system (see Fig. 1), including the anode, cathode, electrolyte, and insoluble products. Additionally, a Pourbaix diagram of the M42 HSS-$H_2PO_4^-$-SO_4^{2-}–H_2O system was constructed to provide a theoretical analysis for the observed electrochemical behavior. Therefore, these combined approaches facilitate a comprehensive exploration of the mechanisms (including corrosion and product formation) for M42 HSS in the H_2PO4^--SO_4^{2-} passivating electrolyte.

3.4.1. Microscopic morphology and composition of the anodic corroded surface

Fig. 5 presents the microscopic morphology of the corroded surface of M42 HSS after anodic polarization in different applied potential regions. Following electrochemical corrosion, the anodic corroded surface of M42 HSS displays significant morphological variations. After active dissolution, the surface develops a uniform and compact corroded product layer, accompanied by the precipitation of numerous M_6C carbide particles and a minimal amount of blocky M_2C carbides (Fig. 5(a)). This phenomenon correlates with the significant decrease in current density observed in Figs. 3(a) and 4(a). As reported by Ge et al. (Ge et al., 2017), carbides do not undergo dissolution during the electrochemical corrosion process. However, compared to the microstructure of M42 HSS before corrosion (see Fig. 2), the darker-appearing carbides exhibit a higher oxygen content (Table 2), suggesting susceptibility to oxidation during the electrochemical corrosion process. Upon reaching the potential E_{FL}, the corroded surface becomes unstable, featuring localized delamination and a porous appearance of exposed corroded products (Fig. 5(b)). This supports the breakdown response observed in oxidation peaks C1 and C2, as shown in Fig. 4, attributed to defects in the corroded product layer. Nevertheless, after the end of passivation, the corroded product layer primarily exhibits microcracks, which have expanded under specific conditions due to corrosion along grain boundaries, resembling a "mud-crack" style, consistent with the literature findings

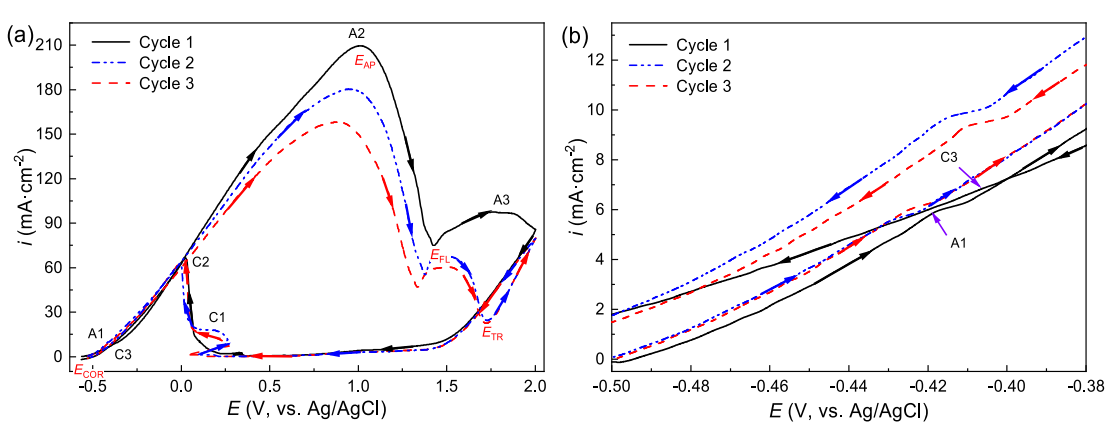

Fig. 4. Cyclic voltammetry curves for M42 HSS in the H_2PO4^--SO_4^{2-} passivating electrolyte at 30 °C: (a) number of cycles, and (b) local enlargement of peaks A1 and C3.

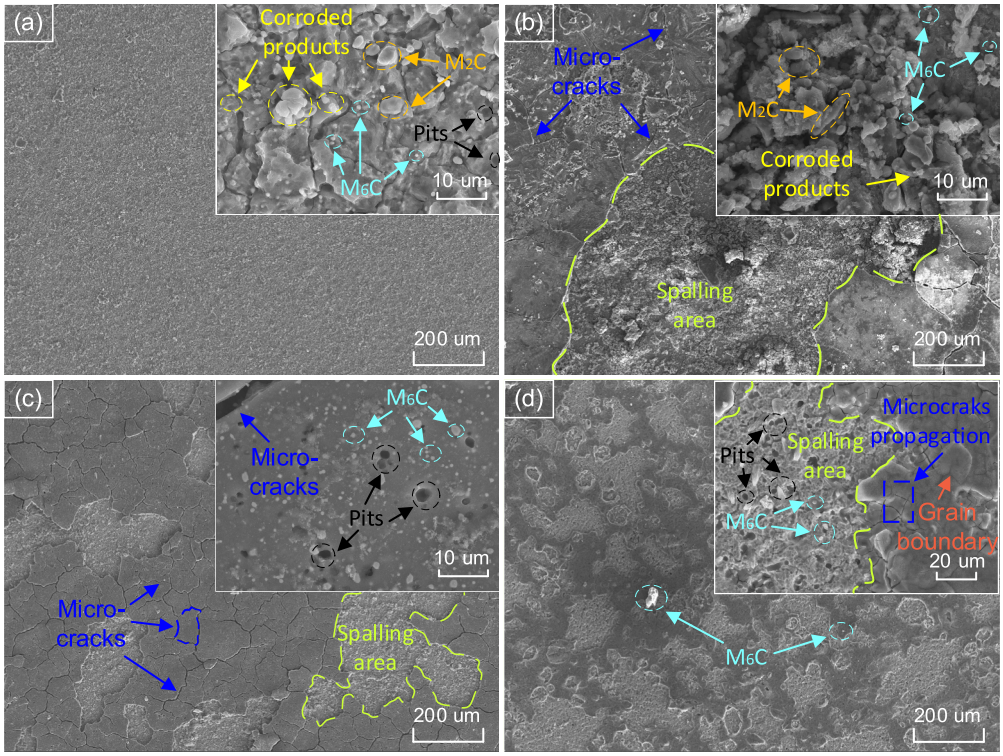

Fig. 5. Microscopic morphology of the corroded surface of M42 HSS after anodic polarization: (a) after active dissolution, (b) after the end of transition, (c) after the end of passivation, and (d) after transpassive dissolution.

Table 2
EDX and thickness results of the corroded surface for M42 HSS after anodic polarization.

Stages	Components	Composition (wt.% ≥ 0.5)										Thickness (μm)
		C	O	P	S	V	Cr	Fe	Co	Mo	W	
After active dissolution	M_6C	12.5	15.7	0.5	0.4	1.5	3.2	27.2	3.2	28.5	6.3	7.30 ± 0.18
	M_2C	12.8	3.5	0.0	0.6	6.9	8.4	5.1	0.4	56.7	5.3	
	Corroded products	2.8	39.1	1.4	0.0	0.4	1.5	39.1	4.1	10.5	0.7	
After the end of transition	M_6C	6.2	15.1	1.7	0.8	1.6	4.4	28.1	3.5	31.5	6.6	15.23 ± 0.31
	M_2C	9.0	18.9	0.8	0.9	6.6	5.0	4.9	0.3	47.0	6.3	
	Corroded products	3.9	32.5	7.9	3.5	1.9	8.3	24.4	2.0	13.1	2.1	
At the end of passivetion	M_6C	6.5	14.3	1.6	0.7	1.9	3.5	25.5	3.0	35.4	6.7	13.65 ± 0.27
	Corroded products	4.9	39.1	10.9	0.9	1.6	7.2	21.0	1.4	11.3	1.2	
After transpassive dissolution	M_6C	5.0	18.1	3.6	0.3	0.5	2.9	58.5	6.3	3.4	0.6	0.64 ± 0.19
	Corroded products	2.9	36.9	14.3	0.7	0.3	1.6	35.1	5.4	2.4	0.2	
	Spalling zone	0.3	3.6	3.1	0.3	0.9	3.9	74.5	8.1	3.1	1.7	

(Ripoll et al., 2016). These microcracks may be associated with internal stresses enhancement (Liu et al., 2023) or dehydration (Wang et al., 2022b) in the corroded product layer. Moreover, oxygen bubble-induced disturbances may lead to poor adhesion between the corroded product layer and the matrix. Localized dissolution of the corroded product layer is observed in the electrolyte, resulting in localized delamination areas and a decrease in layer thickness. Additionally, unpeeled corroded product layer surfaces display pits, likely remnants of detached carbide or oxide particles (Fig. 5(c)), providing effective corrosion pathways for the matrix. These observations help explain the minor fluctuations in current density in the passive region observed in Fig. 3(a), as well as the emergence of oxidation peak A3 in Fig. 4(a). Beyond the potential E_{TR}, an increase in applied potential results in significant spalling within the corroded product layer, ultimately leading to the formation of a new colony-like corroded surface. This progressive spalling ultimately decreases the thickness of the corroded product layer, with the new layer measuring at 0.64 μm. Unfortunately, after transpassive dissolution, the exposed corroded surface exhibits numerous pits with dimple-like features (Fig. 5(d)), likely resulting from a synergistic effect involving pitting corrosion and the detachment of carbide (or oxide) particles. Furthermore, isolated micro-protrusions may be attributed to insufficient removal of residual carbides particles from the surface of the corroded product layer due to bubble-induced disturbances.

To determine the chemical composition and distribution on the surface of the corroded product layer, Fig. 6 shows the XPS full spectrum of the corroded product layer surface of M42 HSS after anodic polarization in different applied potential regions. It is apparent that the corroded surface of M42 HSS lacks detectable levels of certain elements, notably V, Mn, Ni, and W, with particular emphasis on the absence of W and V. Although the content of W and V elements in the M42 HSS matrix is already much lower than that in the carbides, the microscopic morphology and EDX results (see Fig. 5 and Table 2) of the corroded surface suggest that the carbides act as cathodes and the matrix as anodes, resulting in a lower W and V content in the corroded products. These elements are likely dissolved into the electrolyte, a point which will be discussed in greater detail later. Consequently, the contribution of these elements to the corroded products is considered negligible.

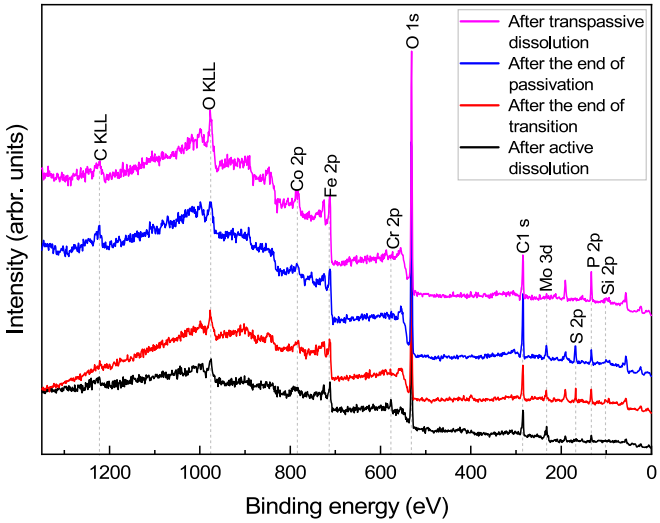

Fig. 6. XPS survey of the corroded product layer's surface of M42 HSS.

Among non-metallic elements, carbon is observed. Although some carbon may have been introduced as contamination during the detection process, the presence of carbides in the corroded products is also a contributing factor, as shown in Table 2. Moreover, Table 3 provides the compositional percentages of the corroded product layer's surface, as determined by XPS analysis. Compared to the results from the last three applied potential regions, the corroded products show the highest proportions of Mo and Cr elements after active dissolution, while the proportion of Co and Fe elements tend to display a general upward trend.

Based on the composition analysis described above, Fig. 7 presents the primary elemental distribution on the surface of the corroded product layer of M42 HSS. Compared to the relatively uniform distribution of elements on the unpeeled surface of corroded product layer after the end of passivation (Fig. 7(c)), the corroded product layer's surface after active dissolution is not uniform (Fig. 7(a)), with significantly lower content of elements such as Fe and Mo in some regions. After the end of transition (Fig. 7(b)), the outer surface of the corroded product layer is rich in P, O, and Cr, suggesting an enrichment of Cr phosphate or oxide in the outer layer. In the delaminated areas of exposed porous corroded products, the composition includes P, S, O, Mo, Fe, Co, and Cr. During transpassive dissolution, a substantial portion of the corroded product layer delaminates, exposing a new corroded surface rich in Fe, Co, and Cr, surrounded by a colony-like structure with high content of P, S, O, Mo, Fe, and Co (Fig. 7(d)). Notably, Cr-containing compounds appear less prevalent compared to the outer layer of the Cr-rich corroded product layer observed after the end of transition, which might seem contradictory at first glance. This apparent discrepancy will be further addressed in subsequent sections. Therefore, these observations indicate that the corroded product layer is composed of phosphates, sulfates, and oxides (or hydroxides). However, the limitations of surface spectroscopy techniques, which do not allow for detailed layering information of the corroded product layer, suggest that further characterization techniques such as Focused Ion Beam (FIB) or Transmission Electron Microscopy (TEM) could provide more insights into the structure and composition for the corroded product layer. Overall, variations in applied potential lead to differences in the composition and distribution of the corroded product layer, indicating the further research is required to thoroughly illustrate how variations in applied potential influence the formation of the corroded product layer and the chemical state of its constituent components.

3.4.2. *Thermodynamic analysis of the M42 HSS-$H_2PO_4^-$-SO_4^{2-}–H_2O system*

Many current studies primarily use spectroscopic techniques to examine corroded products of metals and their alloys in specific media environments (Zeng et al., 2020; Zhou et al., 2021), aiming to determine the types and formation mechanisms of corroded products in a given system. However, these results have been met with controversies. The Pourbaix diagram is widely recognized as a powerful tool in the field of electrochemical corrosion. Initially designed for pure metals, the diagram is often applied to alloys in practical engineering by superimposing individual Pourbaix diagram of the alloy's metallic elements to evaluate electrochemical corrosion behavior in specific media environments (Zhao et al., 2019; Wang et al., 2020). The construction of the Pourbaix diagram depends on minimizing the Gibbs free energy of the system, typically under conventional corrosion limit concentrations (10^{-6} mol·L^{-1}). However, there are exceptions, such as nuclear environments, where the limit concentration is set at 10^{-8} mol·L^{-1} (Zhao et al., 2019; Chen et al., 2021). As discussed in Section 3.4.1, it is imperative to investigate the potential local (or overall) dissolution of oxides or hydroxides in weak acidic environments (Han et al., 2016; Entezari-Zarandi et al., 2020). Additionally, understanding the product formation of sulfate and phosphate salts containing $H_2PO_4^-$, HPO_4^{2-}, PO_4^{3-}, and SO_4^{2-} and determining the stable corroded products under specific applied potential conditions is crucial. Due to the stability of sulfate as an anion and its role as a non-oxidizing agent (El-Naggar, 2006), sulfate reduction primarily occurs in strongly reducing environments (Xia and Luo, 2019). In aqueous environments containing phosphate ions, phosphates generally form in strongly protonated forms such as $H_2PO_4^-$, HPO_4^{2-}, and PO_4^{3-} (Cetiner et al., 2005; Sahoo and Balasubramaniam, 2008). Consequently, in aqueous environments containing phosphates or sulfates, these ions are commonly viewed as ligands for metals (Jing et al., 2019; Bonola et al., 2022). Furthermore, the corrosion of multi-element alloys in specific aqueous environments may lead to the formation of spinel oxides, such as $FeCr_2O_4$ (Liu et al., 2011).

Based on the above discussion, the Pourbaix diagram for the M42 HSS-$H_2PO_4^-$-SO_4^{2-}–H_2O system at 30 °C can be constructed by superimposing five ternary diagrams (Fe-Mo-H_2O, Fe-Co-H_2O, Fe-Cr-H_2O, Mo-Co-H_2O, and Co-Cr-H_2O) to form the Pourbaix diagram of the Fe-Mo-Co-Cr-H_2O system, along with four quaternary diagrams (Fe-$H_2PO_4^-$-SO_4^{2-}–H_2O, Mo-$H_2PO_4^-$-SO_4^{2-}–H_2O, Co-$H_2PO_4^-$-SO_4^{2-}–H_2O, and Cr-$H_2PO_4^-$-SO_4^{2-}–H_2O). This approach captures the complex interactions among the various alloying elements and the phosphate and sulfate environments. Notably, the primary reactions that may occur in the M42 HSS-$H_2PO_4^-$-SO_4^{2-}–H_2O system were enumerated in Table S.3 (Supplementary material). Furthermore, the thermodynamic relationships at 30 °C (303.15 K) were determined using previously reported thermodynamic data (Table S.4, Supplementary material).

Fig. 8(a) shows the Pourbaix diagram of the primary metallic elements in M42 HSS within a salt-free aqueous environment at 30 °C (i.e., the Fe-Mo-Co-Cr-H_2O system). This Pourbaix diagram was constructed

Table 3
Compositional percentages of the corroded product layer's surface of M42 HSS.

Stages	Composition percentages (%)							
	C 1 s	O 1 s	P 2p	S 2p	Fe 2p	Mo 3d	Co 2p	Cr 2p
After active dissolution	21.30	32.26	11.36	0	15.60	10.35	4.98	4.15
After the end of transition	13.80	34.99	11.47	3.49	22.44	4.08	6.98	2.75
After the end of passivation	13.28	33.38	15.29	8.27	19.33	3.09	5.13	2.23
After transpassive dissolution	13.95	35.02	14.07	0	24.03	1.15	9.77	2.01

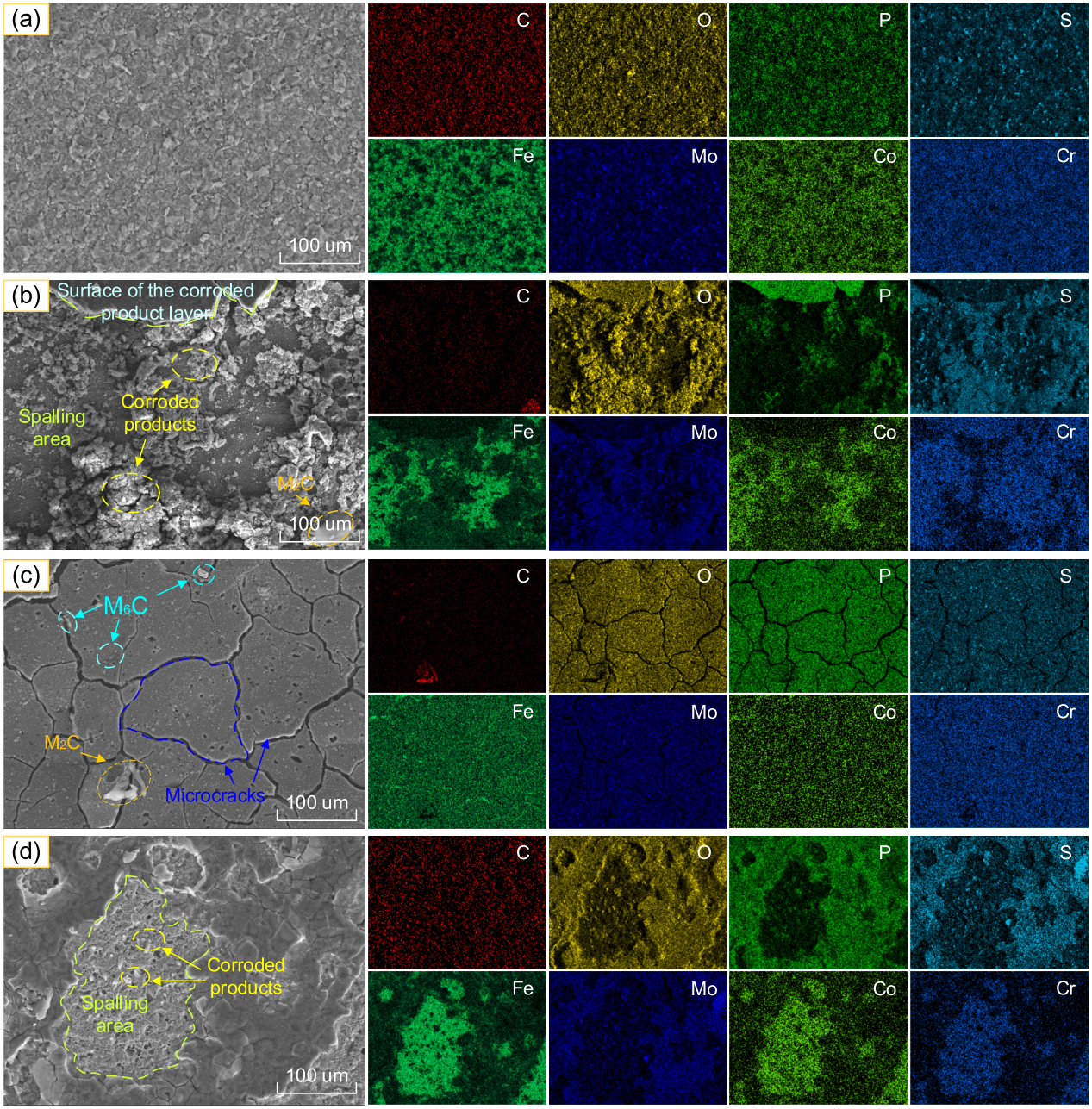

Fig. 7. Elemental distribution on the surface of the corroded product layer of M42 HSS: (a) after active dissolution, (b) after the end of transition, (c) after the end of passivation, and (d) after transpassive dissolution.

by superimposing five ternary diagrams (Fe-Mo-H_2O, Fe-Co-H_2O, Fe-Cr-H_2O, Mo-Co-H_2O, and Co-Cr-H_2O), each presented separately in Fig. S.1 (Supplementary material). For clarity in the following text, "g", "aq", and "s" in the parenthesis represent gas, water-soluble substances (including ions and compounds), and solid substances, respectively; Unless otherwise noted, these designations for substances are often omitted. It can be found in Fig. 8(a) that at a pH of 4.2 (marked by the grey dashed line), Fe and Co undergo dissolution at low potentials but form oxides or hydroxides at higher potentials. In contrast, Mo and Cr form stable oxides at low potentials but become ionic at higher potentials. However, compared to the salt-free aqueous environment, M42 HSS displays distinct species in the $H_2PO_4^-$-SO_4^{2-} passivating electrolyte (Fig. 8(b)). As mentioned above, the Pourbaix diagram for the M42 HSS-$H_2PO_4^-$-SO_4^{2-}–H_2O system at 30 °C was constructed by the superimposing method, with the quaternary diagrams presented in Fig. S.2 (Supplementary material). In Fig. 8(b), it is evident that at low potentials, SO_4^{2-} forms water-soluble $FeSO_4$ with Fe, whereas at high potentials, the stable region of FeO·OH/Fe_2O_3 becomes narrower, allowing for the formation of stable $FePO_4$ precipitates. Under low potentials, both Co and Cr form stable water-soluble sulfates (i.e., $CoSO_4$(aq), $CrSO_4$(aq), and $CrSO_4^+$) in complexed with SO_4^{2-}, while Cr-containing oxides are less likely to precipitate; At high potentials, the stable region of Co-containing and Cr-containing products (including Co_3O_4, $Co(OH)_3$, and $HCrO_4^-$) remains nearly relatively unchanged. Notably, spinel oxides such as Fe_3O_4, $FeCr_2O_4$, CoO·Fe_2O_3, and $CoCr_2O_4$ exhibit stability under low potentials and are resistant to the effects of neutral or alkaline environments. For Mo in aqueous environments, both Alamdari et al. (Alamdari and Sadrnezhaad, 2000) and Entezari-Zarandi et al. (Entezari-Zarandi et al., 2020) reported the formation of complex compounds such as $Mo_2O_5(SO_4)_2^{2-}$ and MoO_2SO_4 in association with SO_4^{2-}, but the absence of thermodynamic data for these compounds complicates their analysis in the M42 HSS-$H_2PO_4^-$-SO_4^{2-}–H_2O system.

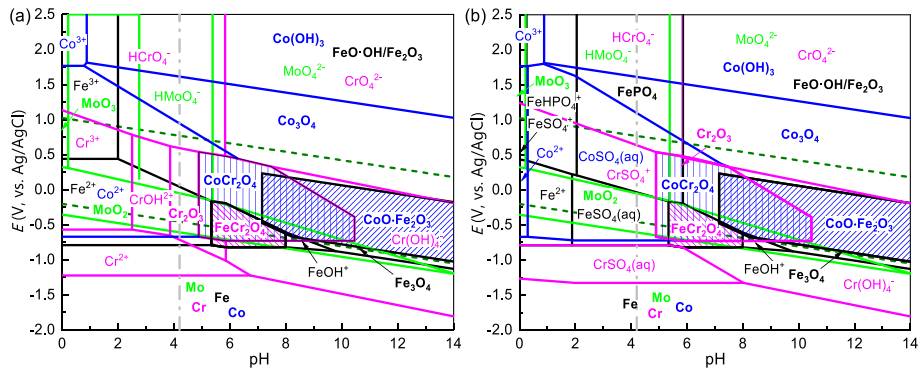

Fig. 8. Pourbaix diagrams at 30 °C of: (a) the Fe-Mo-Co-Cr-H_2O system; (b) the Fe-Mo-Co-Cr-$H_2PO_4^-$-SO_4^{2-}–H_2O system (named the M42 HSS-$H_2PO_4^-$-SO_4^{2-}–H_2O system). $[M(aq)]_{tot.} = 10^{-6}$ mol·L^{-1} (M=Fe, Mo, Co, and Cr), $[H_2PO_4^-] = 1.217$ mol·L^{-1}, and $[SO_4^{2-}] = 0.282$ mol·L^{-1}.

Yao et al. (Yao et al., 2018) also noted that Mo enhanced the resistance of tungsten-cobalt alloys to non-oxidizing acids such as HCl and H_2SO_4, primarily forming oxides rather than ions. However, no information has been reported regarding Mo-containing complex products in aqueous environments with phosphate ions. As a result, the Mo-$H_2PO_4^-$-SO_4^{2-}–H_2O system simplifies to the Mo-H_2O system. At low potentials, Mo oxides to form MoO_2, while at higher potentials, it primarily exists as $HMoO_4^-$. In conclusion, from a thermodynamic analysis perspective, these findings suggest the corrosion behavior and dominant products for M42 HSS in the $H_2PO_4^-$-SO_4^{2-} passivating electrolyte can vary with changes in applied potential, highlighting the elemental distribution differences by varying potential levels, as discussed in Section 3.4.1. However, to accurately identify the likely dominant products of the M42 HSS-$H_2PO_4^-$-SO_4^{2-}–H_2O system, further research is required using spectroscopic techniques.

3.4.3. Component analysis of anodic corroded products

Fig. 9 presents the XRD results for M42 HSS both before and after corrosion. Before corrosion, two eutectic carbide precipitates, M_2C and M_6C, are identified within the matrix, consistent with the EDX results of M42 HSS (see Fig. 2). After active dissolution, the corroded products on the surface of M42 HSS primarily consist of FeO·OH, $FePO_4$, MoO_3, and Cr_2O_3, along with eutectic carbide precipitates, but without spinel oxides. As the polarization process continues, the intensity of the characteristic peaks gradually diminishes, particularly after the end of transition, ultimately resulting in the near disappearance of characteristic peaks corresponding to MoO_3 and Cr_2O_3. This observation can be explained through the thermodynamic analysis described in the preceding section. Beyond a certain applied potential, the stability of Cr-containing and Mo-containing oxides and in the corroded product layer is compromised, causing localized dissolution of the corrosion layer in certain areas. After transpassive dissolution, the corroded product layer undergoes significant delamination or partial dissolution, and the exceedingly thin corroded product layer falls below the XRD detection threshold, exposing only the matrix phase. As reported by Alves et al. (Alves et al., 2001), corroded product films on alloy surfaces are often thin, making it challenging to accurately determine crystal structure properties due to low-intensity diffraction peaks. Moreover, the presence of some amorphous composition within the corrosion products might contribute to variations in peak intensity (Anwar et al., 2023). These could explain why Co-containing compounds in the corroded products at high potentials are difficult to discern. Furthermore, XRD analysis has limitations in definitively identifying solid phases of Mo-containing sulfates, potentially due to their low concentration, leading to non-detection in the patterns.

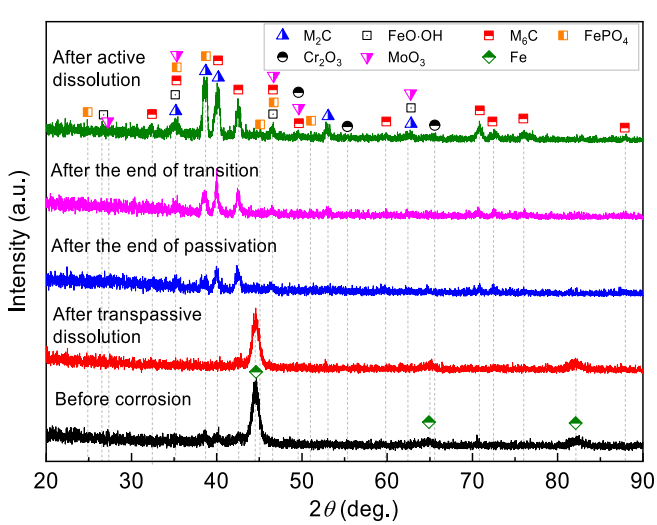

Fig. 9. XRD results of M42 HSS both before and after corrosion.

To comprehensively characterize the corroded products formed on the surface of M42 HSS in the $H_2PO_4^-$-SO_4^{2-} passive electrolyte, XPS was carried out to gain more detailed information for the corroded product layer. Notably, for such uneven surfaces, repeated measurements consistently yielded identical XPS spectra for the corroded product layer of M42 HSS. Based on the composition analysis of the corroded product layer of M42 HSS after anodic polarization in different applied potential regions (see Fig. 6), Fig. 10 depicts the elemental XPS spectra of the corroded products. Noise peaks observed in elements such as Cr may result from surface non-uniformity or low content. Moreover, due to the complex nature of the chemical state for O 1 s spectrum, peak fitting is conventionally performed using OH^- (which partially coincides with the PO_4^{3-} peak), O^{2-} (representing metal oxides), and H_2O (which overlaps with the SiO_2 peak) (Tardio et al., 2015). For passivating elements such as Fe, Co, and Cr, which are characterized by multiple split peaks, the chemical states are typically fitted in conjunction with their satellite peaks (Biesinger et al., 2011). Furthermore, the P 2p spectrum has closely spaced spin–orbit components ($\Delta = 0.87$ eV), typically requiring a single peak for fitting (Huang et al., 2019). Binding energies of each component in these spectra are derived from Biesinger's research (Biesinger et al., 2011) and the NIST XPS database (Naumkin et al., 2023).

The XPS analysis results in Fig. 10(a) indicate that, the C 1 s spectrum primarily arises from inadvertent contamination during the detection process. Meanwhile, the presence of carbides like Mo_2C is consistent with observations from the EDX-mapping and XRD results (see Figs. 7 and 9). The peak fitting analysis of the P 2p spectrum (Fig. 10(c)) confirms the presence of $FePO_4$ and $CrPO_4$ in the corroded products. The existence of $FePO_4$ is consistent with thermodynamic predictions and XRD results. However, the presence of $CrPO_4$ remains inconclusive due to the current lack of thermodynamic data for $CrPO_4$(s) and the low chromium content in M42 HSS. Fortunately, after the end of transition and transpassive dissolution stages, Fig. 7(b) and (c) show that the outer

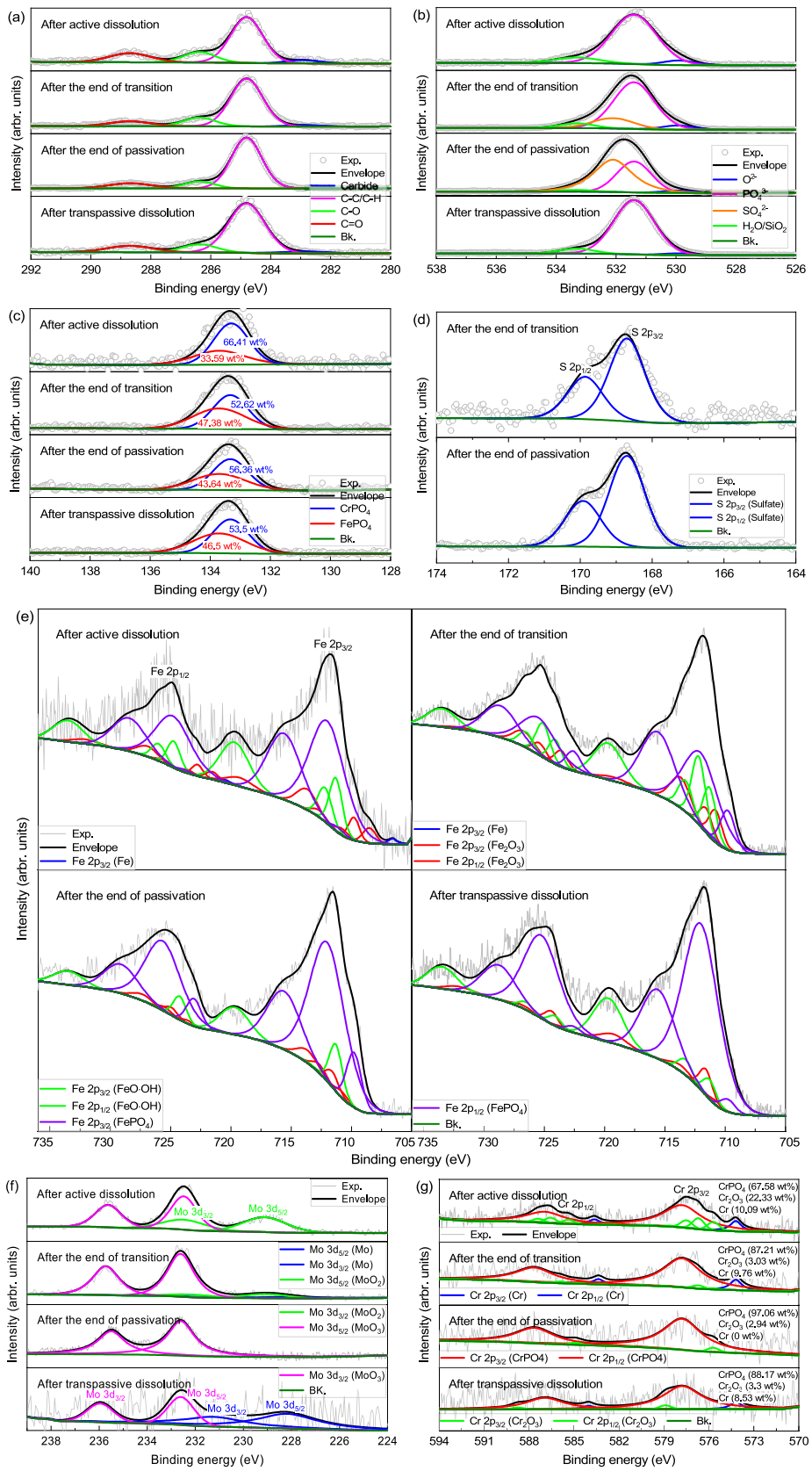

Fig. 10. XPS analysis results of the corroded product layer's surface of M42 HSS after anodic polarization: (a) C 1 s, (b) O 1 s, (c) P 2p, (d) S 2p, (e) Fe 2p, (f) Mo 3d, (g) Cr 2p, and (h) Co 2p.

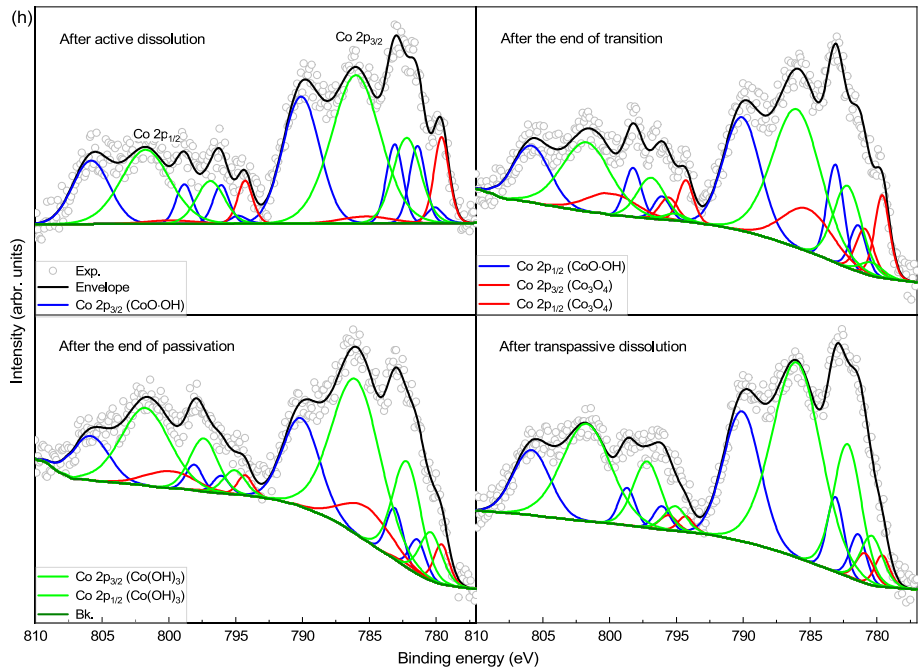

Fig. 10. (*continued*).

surface of the corroded product layer is rich in Cr, P, and O, with relatively diminished Fe, suggesting the presence of $CrPO_4$. Notably, the peak intensity proportion for $CrPO_4$ is higher than that for $FePO_4$. A plausible explanation for this outer layer enrichment of the corroded product layer could be the lower Gibbs free energy of $FePO_4$ ($Fe^{3+} + H_2PO_4^- \rightarrow FePO_4 + 2H^+$, $\Delta G(298.15) = -35.98$ kJ·mol^{-1}) compared to $CrPO_4$ ($Cr^{3+} + H_2PO_4^- \rightarrow CrPO_4 + 2H^+$, $\Delta G(298.15) = -33.85$ kJ·mol^{-1}) (Vieillard and Tardy, 1984), which promotes the rapid formation of $FePO_4$ in the inner layer, allowing for the gradual accumulation of $CrPO_4$ in the outer layer. Giver that Na is not detected in the corroded products (see Fig. 6), the emergence of a distinct S 2p spectrum (Fig. 10(d)) after the end of transition and passivation stages suggests the presence of SO_4^{2-} moieties (Bai et al., 2021), possibly derived from sulfates like $FeSO_4$ (Yue et al., 2018; Bai et al., 2021), rather than Na_2SO_4. Although the thermodynamic analysis reveals that $FeSO_4$(s) is unlikely to form in the system, $FeSO_4$(aq) might still be produced (Lu and Chen, 2000). Additionally, the EDX-mapping results in Fig. 7(b) show that corroded products are rich in S and Mo. As reported by Alamdari et al. (Alamdari and Sadrnezhaad, 2000), Mo(VI) can form complexes with SO_4^{2-}, such as MoO_2SO_4. Unfortunately, the absence of binding energy data for this specific sulfate complicates its identification in the S 2p and Mo 3d spectra (Fig. 10(f)). Bai et al. (Bai et al., 2021) reported the formation of Fe_2O_3 and FeO·OH as corroded products on the steel surface in Na_2SO_4. Considering the P 2p spectrum and XRD analysis results, the Fe 2p spectrum in Fig. 10(e) indicates the presence of $FePO_4$, FeO·OH, and Fe_2O_3 in the corroded products, aligns with the types of iron-based substances identified in the thermodynamic analysis. Regarding Mo, although XPS analysis fails to identify peaks of Mo-containing sulfate compounds after the end of transition and passivation stages, the confirmation of MoO_2 and MoO_3 in the Mo 3d spectrum of the corroded products is consistent with the corroded products of Mo-containing 316 stainless steel in an H_2S corrosion environment, as reported by Shah et al. (Shah et al., 2020). Notably, an intriguing observation is that the peak intensity of MoO_2 in the corroded products detected in the last three applied potential regions gradually decreases until it disappears. This phenomenon can be explained by the thermodynamic analysis, indicating that as the applied potential increases a certain potential value, MoO_2 becomes unstable and prone to dissolution. The analysis results from EDX-mapping and P 2p spectrum confirm the presence of $CrPO_4$ in the corroded products, while the XRD results reveal the presence of Cr_2O_3. Therefore, the Cr 2p spectrum consists of Cr-containing carbides, $CrPO_4$, and Cr_2O_3 peaks (Fig. 10(g)). The relative peak intensities suggest $CrPO_4$ is the predominant form of Cr(III), with Cr_2O_3 appearing in a lower proportion. Notably, after active dissolution, the proportion of Cr_2O_3 in the Cr 2p spectrum is significantly higher compared to the results from the last three applied potential regions. As reported by Han et al. (Han et al., 2023), the stability of $CrPO_4$ exceeds that of $Cr(OH)_3$ and Cr_2O_3, indicating that when the applied potential exceeds the potential E_{AP}, Cr-containing corroded products are primarily composed of $CrPO_4$, while Cr_2O_3 becomes less table and prone to dissolution. Additionally, Fig. 7(b) suggests that the outer layer of the corroded product is rich in $CrPO_4$ or Cr_2O_3, but Fig. 7 (d) shows that the regions with high P and O contents have low Cr content. A plausible explanation is that in the transpassive dissolution region, the corroded product layer undergoes gradual spalling, exposing the alloy surface and initiating the formation of a new, exceptionally thin corroded product layer. In this context, the competition between $FePO_4$ and $CrPO_4$ becomes evident, leading to diminished Cr content in regions of the outer corroded product layer that are rich in P and O. For Co, conventional synthesis methods for CoO·OH and Co_3O_4 involve Co^{2+} reactions in aqueous environments (Figlarz et al., 1974; Yang et al., 2010). Moreover, a research by Schubert et al. (Schubert et al., 2013) indicates that the anodic dissolution of Co leads to the formation of Co (II, III) oxide (Co_3O_4), which subsequently undergoes hydrolysis, resulting in the formation of $Co(OH)_3$. However, the current lack of thermodynamic data for CoO·OH calls for further refinement by thermodynamics researchers. Consequently, this species is not presented in the Pourbaix diagram of the system. Although the absence of Co-containing compounds in XRD, the combined evidence from thermodynamic analysis and previous research suggests that, after anodic polarization in different applied potential regions, the corroded products include CoO·OH, Co_3O_4, and $Co(OH)_3$ (Fig. 10(h)).

In summary, from the analysis and discussion of the corroded product layer's surface of M42 HSS, it can be apparent that as the applied potential increases, Mo-containing and Cr-containing compounds (such as MoO_2 and Cr_2O_3) tend to become increasingly unstable and prone to dissolution, whereas Co-containing and Fe-containing precipitates not only continue to form at high potentials but also

become progressively stable. Therefore, the Pourbaix diagram for the M42 HSS-$H_2PO_4^-$-SO_4^{2-}–H_2O system suggests that variations in applied potential lead to form distinct types of corroded products, a finding validated by the analysis results from XRD and XPS.

3.4.4. Analysis of the used electrolytes

Fig. 11(a) illustrates the concentration distribution of metallic elements in the used electrolyte after anodic polarization in different applied potential regions. In response to applied potential, metallic elements in M42 HSS are released from the anode, with their concentrations resulting from various electrochemical processes that lead to the formation of metal ions or water-soluble substances. The dissolution of Mn, V, Ni, and W in M42 HSS into the electrolyte is clearly observed, as confirmed by previous analyses of the composition of corroded products. It is noteworthy that although the higher content of V and W in M42 HSS compared to Mn (see Table S.1, Supplement material), the extent of their dissolution into the electrolyte is significantly lower than that of Mn. The Microstructural examinations of M42 HSS (see Fig. 2), along with EDX results from the corroded products summarized in Table 2, indicate that V and W elements are primarily contained within carbide precipitates, which likely accounts for their lower solubility. Although the content of Ni is comparable to that of Mn in M42 HSS, its extent of dissolution into the electrolyte is less significant. This discrepancy can be explained by the more negative standard electrode potential of Mn, which promotes its preferential dissolution. Furthermore, although the content of V and W in M42 HSS is nearly equivalent, and even though W has higher proportion than V in the M_2C and M_6C carbides as well as in the matrix, the dissolution content of W into the electrolyte is higher than that of V. This suggests that the likely presence of V-rich carbides with a non-stoichiometric ratio may exist in M42 HSS, as reported in previous studies (Serna and Rossi, 2009; Qu et al., 2012).

Subsequently, the dissolution content of Fe, Mo, Co, and Cr is primarily discussed. The Pourbaix diagram for the M42 HSS-$H_2PO_4^-$-SO_4^{2-}–H_2O system, presented in Fig. 8(b), reveals that during the early stages of active dissolution, as the applied potential increases from the potential E_{COR} to −0.06 V, Cr begins to dissolve ahead of Mo, resulting in the formation of Cr-containing oxides. However, in the presence of SO_4^{2-}, Cr_2O_3 dissolves into the electrolyte as $CrSO_4^+$, while the dissolution of Fe and Co continues. In the later stages of active dissolution, MoO_2 undergoes further oxidation, leading to the formation of MoO_3 and $HMoO_4^-$, while $FePO_4$ continues to evolve, as shown in Fig. 11(b). Although the higher Mo content in M42 HSS compared to Co and Cr, its dissolution content is approximately equivalent to that of Co and Cr. This is primarily due to the formation of MoO_2 and the presence of Mo-rich carbides. In the applied potential range between E_{AP} and E_{FL}, Cr-containing ions and oxides undergo further oxidation to form $HCrO_4^-$. Moreover, significant dissolution of MoO_2 and Cr_2O_3 occurs in the corroded product layer, contributing to its porous structure, as observed in Figs. 5(b) and 7(b). This less dense corroded product layer facilitates the subsequent corrosion of other elements like Fe and Co. After the end of transition, the dissolution rate of elements Fe, Mo, Co, and Cr increases rapidly (Table 4). As the applied potential increases to the potential range of E_{FL} and E_{TR}, Co-containing water-soluble species continue to form Co_3O_4, and MoO_2 in the corroded products is completely dissolved, as presented in Fig. 10(f). In both spalling and unpeeled areas (see Fig. 5(c)), the dense corroded product layer significantly slows the dissolution of the alloy, resulting in a relatively gradual increase in their concentration in the electrolyte after the end of passivation. Furthermore, beyond the potential E_{TR}, although the spalling observed in the corroded product layer of M42 HSS, numerous insoluble corrode products, such as $FePO_4$ and $Co(OH)_3$, remain in the spalling areas or on the surface of the corroded product layer, contributing to an extremely slow rate of dissolution for these elements after transpassive dissolution (around 1200 s). Therefore, the concentrations of Fe, Mo, Cr, and Co elements in the electrolyte initially increase rapidly and then grow more gradually, affirming that the dissolution of alloy/passive film is influenced by both the applied potential and time (Fredriksson et al., 2012; Wongpanya et al., 2022).

3.4.5. Product analysis on the cathodic surface

In the electrochemical corrosion of metals and their alloys, alongside the typical reduction of hydrogen or oxygen (Schmickler and Santos, 2010; Gossenberger et al., 2020), there is a considerable interest in understanding the formation of products on the cathodic surface. Fig. 12 shows the compositional analysis of the Pt sample after anodic polarization. The surface of the Pt sample exclusively displays the presence of Pt and Fe elements, with minimal oxygen content, making it difficult to identify Fe-containing products. To further exam the products on the Pt sample's surface, electrochemical tests using the constant potential testing were conducted. The results show a remarkably thin film of adsorbed products on the Pt sample's surface, and its XPS analysis is presented in Fig. 13. Apart from inherent impurities of Si_3N_4 and SiO_2 in Pt (Fig. 13 (e) and (i)), the adsorbed products contain Fe, Mo, Cr, P, and O. According to electrochemical interface theory (Schmickler and

Table 4
Average dissolution rate of metallic elements in the used electrolyte (mg·(L·s)$^{-1}$).

	Fe	Mo	Co	Cr
After active dissolution	0.171	0.056	0.054	0.059
After the end of transition	0.194	0.073	0.062	0.065
After the end of passivation	0.142	0.052	0.048	0.049
After transpassive dissolution	0.095	0.034	0.033	0.033

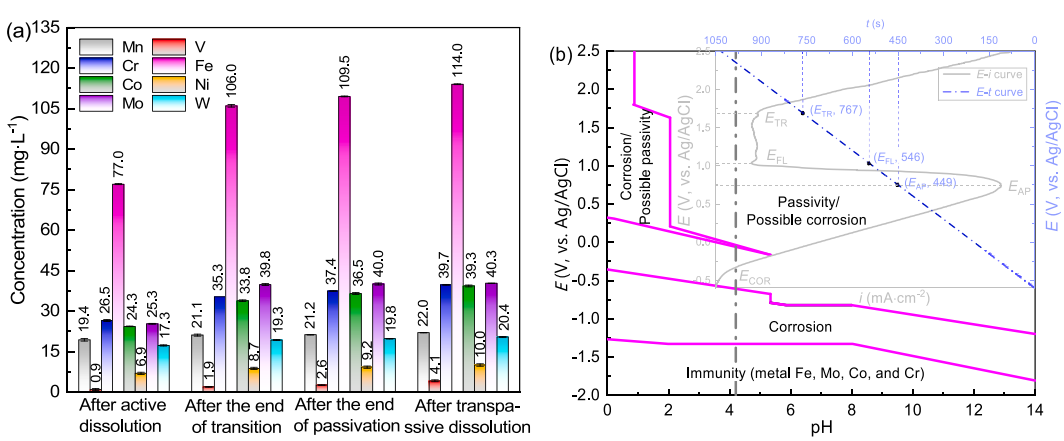

Fig. 11. (a) Concentration distribution of metallic elements in the used electrolyte after anodic polarization and (b) Simplified Pourbaix diagram of the M42 HSS-$H_2PO_4^-$-SO_4^{2-}–H_2O system.

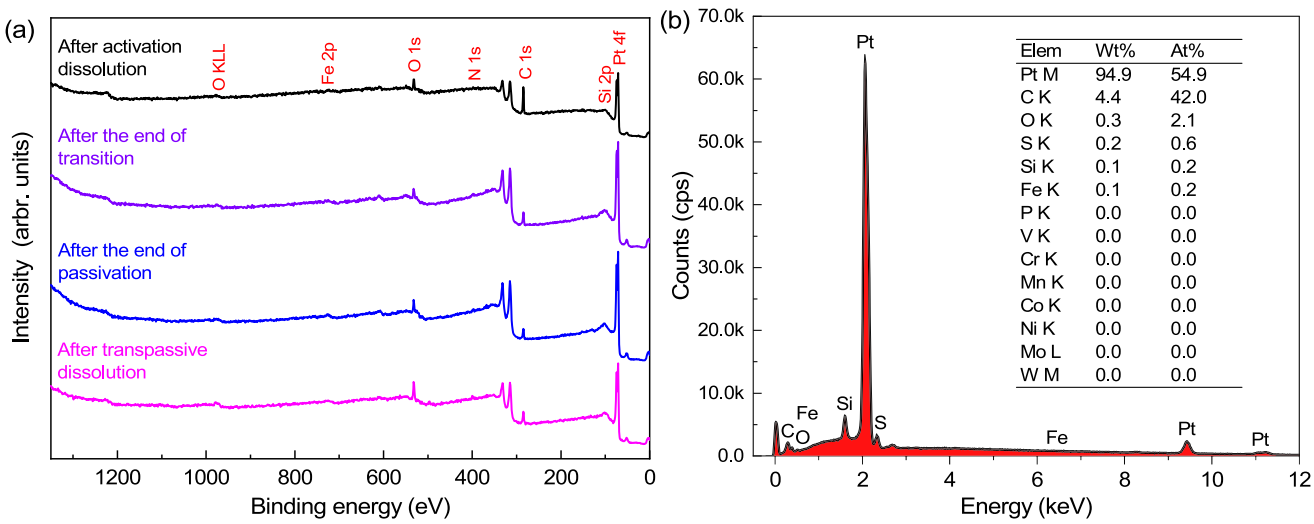

Fig. 12. Composition of the Pt sample: (a) XPS results after anodic polarization in different applied potential regions, and (b) EDX-mapping results after transpassive dissolution.

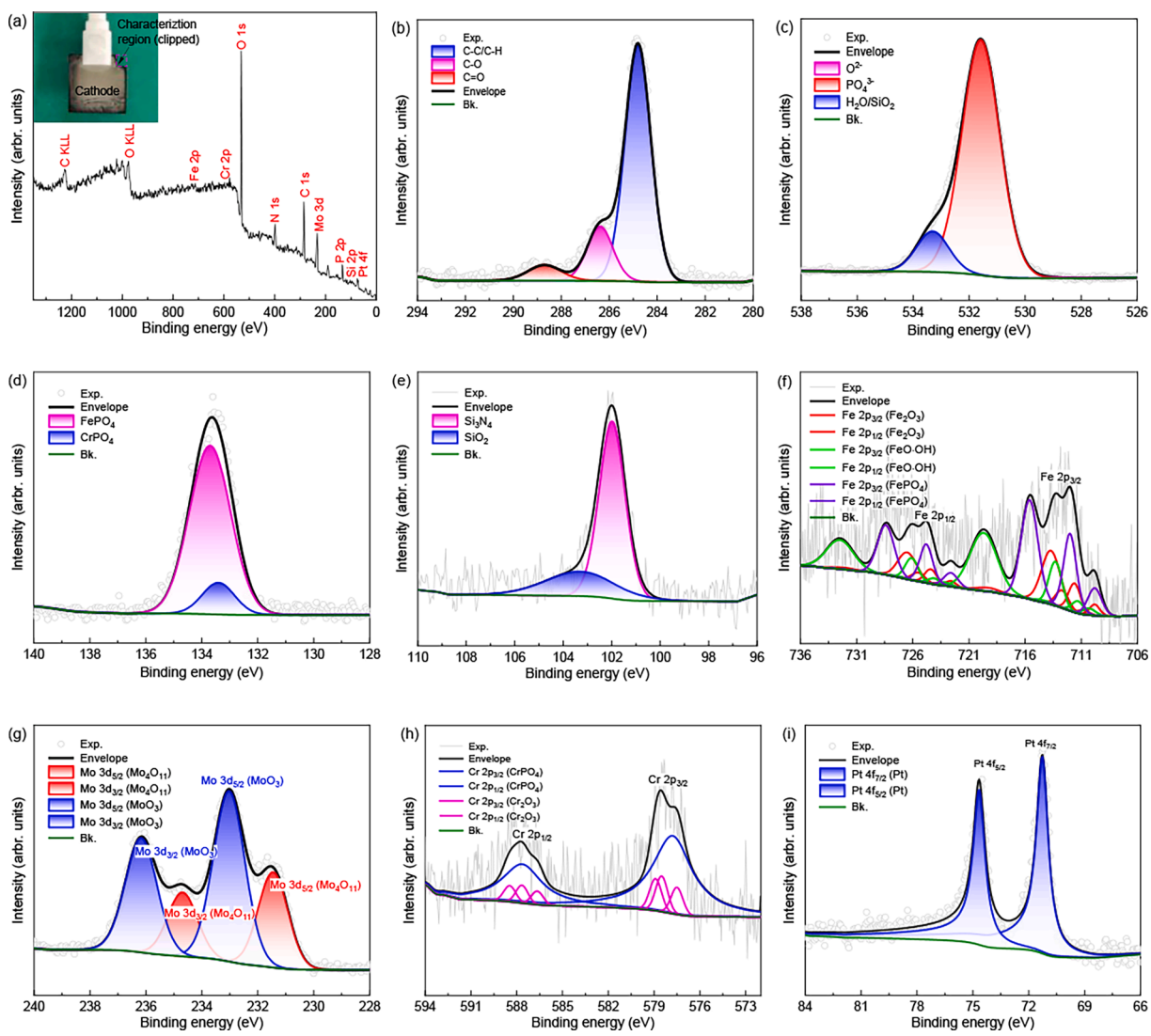

Fig. 13. XPS analysis results of the Pt sample's surface: (a) survey, (b) C 1 s, (c) O 1 s, (d) P 2p, (e) Si 2p, (f) Fe 2p, (g) Mo 3d, (h) Cr 2p, and (i) Pt 4f.

Santos, 2010), charged electrodes attract counterions from the electrolyte. However, in the coexistence of anions, PO_4^{3-} tends to have a stronger adsorption capability than SO_4^{2-} (Guo et al., 2022). Consequently, cations such as Fe^{2+}, Cr^{3+}, and Mo^{3+}, along with anions like OH^- and PO_4^{3-}, may form adsorption phases through robust chemical interactions. In the electrolyte, the stable existence of $Fe(OH)_2$ is unlikely. Therefore, the adsorbed products on the Pt sample's surface primarily consist of phosphate compounds (such as $FePO_4$ and $CrPO_4$) and oxides (such as Fe_2O_3, Cr_2O_3, and MoO_3), while Co-containing oxides and hydroxides are notably absent. This may be because Co^{3+}, with a positive Gibbs free energy (see Table S.4, Supplement material), has reduced adsorption capability on the Pt sample's surface compared to other metal ions, making the formation of containing $Co(OH)_3$ adsorbed products improbable. Furthermore, Co^{2+} is less prone to forming Co_3O_4 under cathodic reduction potentials. However, for the Mo 3d spectrum (Fig. 13(g)), the presence of Mo_4O_{11} among the adsorbed products is plausible (Lyu et al., 2020). Given the considerably stronger adhesion strength of the adsorbed product film on the Pt sample's surface compared to the forces applied during ultrasonic cleaning, there is minimal risk of damage to the cathode tool during electrochemical corrosion machining. Nevertheless, the presence of this adsorbed product film on the cathodic surface could not only impact the cathode's functionality, but also potentially alter the corrosive effects on the anodic workpiece.

3.4.6. Analysis of insoluble products

During the anodic polarization process, the corroded products gradually begin to detach from the surface of M42 HSS after the end of transition, eventually leading to complete detachment and precipitation into the electrolyte in the transpassive dissolution region. To examine the insoluble products in the electrolyte, they were collected, dried, and examined using XRD and XPS, as presented in Fig. 14. The XPS analysis results show that the insoluble products contain non-metallic elements such as C, O, Si, P, S, along with metallic elements like Co, Cr, Fe, Mo, Na (Fig. 14(a)). Since the chemical state of these elements generally aligns with the assessment of the corroded surface of M42 HSS after the end of passivation, further elaboration is unnecessary. However, the composition of the insoluble products is significantly complex (Fig. 14(b)), with some unidentified low-intensity diffraction peaks. It is clear that the insoluble products include various carbides (M_2C and M_6C), oxides, phosphate compounds, and residual electrolytes. Notably, during the anodic polarization process, a minimal quantity of white precipitates was observed in the electrolyte. Additionally, white flocculent precipitates, possibly $Fe(OH)_2$, were also noticed during constant potential electrochemical testing. This occurrence suggests that during the electrochemical corrosion process, H^+ is consumed, leading to an increase in the pH of the electrolyte, resulting in the formation of unstable white flocculent precipitates in the electrolyte. Therefore, the insoluble products not only primarily originate from the corroded products that detached from the anodic surface, but also include a minimal quantity of white precipitates that formed in the electrolyte during the electrochemical corrosion process.

3.5. Mechanisms of product formation and corrosion

3.5.1. Product formation on the cathodic Pt surface

The phenomena observed in Fig. 14(a) during the electrochemical corrosion process suggest that the cathode primarily undergoes reduction reactions, primarily involving the reduction of hydrogen or oxygen in the $H_2PO_4^-$-SO_4^{2-} passivating electrolyte. These reactions can be described by the following reactions (Schmickler and Santos, 2010; Gossenberger et al., 2020):

$$O_2 + 2H_2O + 4e^- \rightarrow 4OH^- \tag{6}$$

$$2H_2O + 2e^- \rightarrow H_2 + 2OH^- \quad (\text{or } 2H^+ + 2e^- \rightarrow H_2) \tag{7}$$

According to standard reduction potentials (Grinon-Echaniz et al., 2021), oxygen reduction ($E = +0.4$ V, vs. SHE) is more likely to occur on the cathodic surface than hydrogen evolution. Over time, the release of OH^- or the consumption of H^+ on the cathodic surface can cause a localized pH change (Barchiche et al., 2003). Consequently, cations adsorbed on the cathodic surface tend to form deposits with anions such as HPO_4^{2-}, PO_4^{3-}, and OH^- in the electrolyte. Furthermore, the electrochemical corrosion process primarily occurs under aerated conditions, where the electrolyte maintains a specific level of oxygen saturation. Based on the analysis of adsorbed products on the Pt sample's surface, it can be inferred that Fe^{2+}/Fe^{3+} adsorbed on the cathodic surface may undergo the following reactions in the $H_2PO_4^-$-SO_4^{2-} passivating electrolyte (Hsiang et al., 2018; Mandal et al., 2020):

$$Fe^{2+} + 2OH^- \rightarrow Fe(OH)_2 \tag{8}$$

$$4Fe(OH)_2 + O_2 \rightarrow 4FeO{\cdot}OH + 2H_2O \tag{9}$$

$$2FeO{\cdot}OH \rightarrow Fe_2O_3 + H_2O \tag{10}$$

$$Fe^{3+} + PO_4^{3-} \rightarrow FePO_4 \tag{11}$$

The formation of Cr-containing deposits on the cathodic surface, specifically $CrPO_4$ and Cr_2O_3, can be explained through Reactions (12) and (13) (Rosas-Becerra et al., 2017; Shah et al., 2020).

$$2Cr^{3+} + 6OH^- \rightarrow Cr_2O_3 + 3H_2O \tag{12}$$

$$Cr^{3+} + H_2PO_4^- \rightarrow CrPO_4 + 2H^+ \tag{13}$$

Moreover, as reported by Lyu et al. (Lyu et al., 2020), under certain

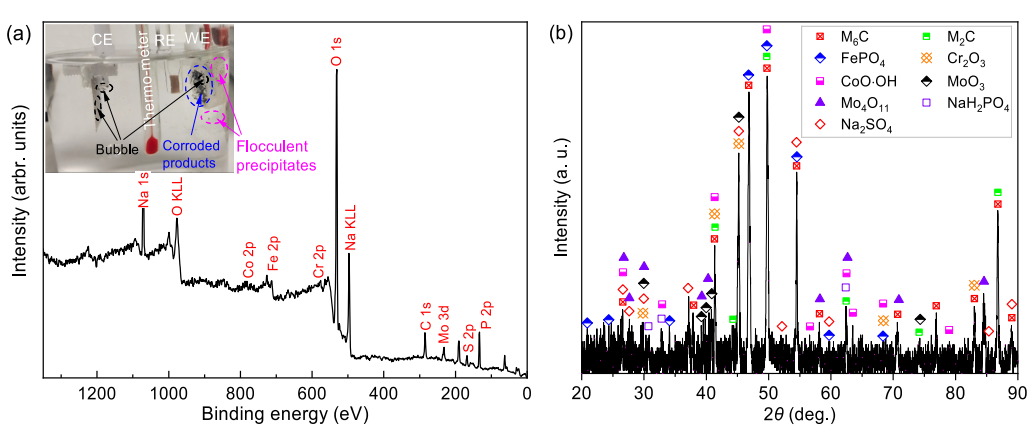

Fig. 14. Results of the insoluble products in the used electrolyte after transpassive dissolution: (a) XPS survey analysis, and (b) XRD analysis.

reduction conditions, MoO_3 can be reduced to Mo_4O_{11}, which may subsequently be reduced to MoO_2. However, the reduction of MoO_2 depends on the pressure and temperature of the investigated system (Schulmeyer and Ortner, 2002). Nevertheless, the absence of MoO_2 in the Mo 3d spectrum on the cathodic surface suggests that MoO_3 formed on the cathodic surface under hydrogen evolution conditions is more prone to convert into Mo_4O_{11}, as shown in Fig. 13(g). The corresponding reactions may be expressed as follows (Dang et al., 2014; Shah et al., 2020):

$$Mo^{6+} + 6OH^- \rightarrow MoO_3 + 3H_2O \quad (14)$$

$$4MoO_3 + H_2 \rightarrow Mo_4O_{11} + H_2O \quad (15)$$

However, in the electrolyte, minimal amounts of flocculent precipitates are formed. The underlying mechanism for these precipitates is closely similar to the process that leads to the formation of adsorbed products on the cathodic surface, as discussed earlier. Furthermore, in the electrolyte containing $H_2PO_4^-$, several other substances may also be produced (Hsiang et al., 2018):

$$H_3PO_4(aq) \leftrightarrow H^+ + H_2PO_4^- \quad (16)$$

$$H_2PO_4^- \leftrightarrow H^+ + HPO_4^{2-} \quad (17)$$

$$HPO_4^{2-} \leftrightarrow H^+ + PO_4^{3-} \quad (18)$$

3.5.2. Product formation on the anodic surface of M42 HSS

As the applied potential increases, M42 HSS displays distinct anodic polarization characteristics in the $H_2PO_4^-$-SO_4^{2-} passivating electrolyte, as shown in Fig. 3(a). These characteristics include regions of active dissolution, transition, passivation, and transpassive dissolution. Moreover, the M42 HSS-$H_2PO_4^-$-SO_4^{2-}–H_2O system exhibits regions denoting immunity, corrosion, passivation, and possible passivation/corrosion, as presented in Fig. 11(b). Therefore, beyond a certain threshold potential, the formation of corroded products begins to hinder further anodic corrosion. Furthermore, when the applied potential exceeds approximately 0.75 V (see Fig. 8), oxygen evolution reactions also occur simultaneously (Lohrengel et al., 2003):

$$2H_2O \rightarrow O_2 + 4H^+ + 4e^- \quad (19)$$

However, these metallic elements in the M42 HSS matrix, including Mn, V, Ni, and W, dissolve directly into the electrolyte as ions, primarily serving a conductive role during the electrochemical corrosion process (Schmickler and Santos, 2010), with minimal contribution to the formation of corroded products.

The corroded products formed on the surface of M42 HSS vary in response to changes in applied potential. As illustrated in the Pourbaix diagram of the M42 HSS-$H_2PO_4^-$-SO_4^{2-}–H_2O system, Cr initially undergoes dissolution to yield Cr^{2+}, some of which subsequently form $CrSO_4$(aq) through complexation with SO_4^{2-}. As the applied potential increases, Cr-containing products are further oxidized to Cr^{3+}, resulting in the formation of Cr_2O_3 and $CrSO_4^+$. However, at an applied potential of approximately 0.67 V, Cr-containing products are ultimately oxidized to $HCrO_4^-$. Additionally, the Cr 2p spectrum of the corroded products on the surface of M42 HSS, as shown in Fig. 10(g), confirms the formation of $CrPO_4$ due to the chelating effect of $H_2PO_4^-$. Therefore, during the electrochemical corrosion process, the formation of Cr-containing products can be summarized as follows (Figlarz et al., 1974; Marcus and Protopopoff, 1997; Bonola et al., 2022):

$$Cr \rightarrow Cr^{2+} + 2e^- \quad (20)$$

$$Cr^{2+} \rightarrow Cr^{3+} + e^- \quad (21)$$

$$2Cr^{2+} + 3H_2O \rightarrow Cr_2O_3 + 6H^+ + 2e^- \quad (22)$$

$$Cr + SO_4^{2-} \rightarrow CrSO_4(aq) + 2e^- \quad (23)$$

$$CrSO_4(aq) \rightarrow CrSO_4^+ + e^- \quad (24)$$

$$Cr^{3+} + H_2PO_4^- \rightarrow CrPO_4 + 2H^+ \quad (25)$$

$$Cr_2O_3 + 5H_2O \rightarrow 2HCrO_4^- + 8H^+ + 6e^- \quad (26)$$

$$CrSO_4^+ + 4H_2O \rightarrow HCrO_4^- + SO_4^{2-} + 7H^+ + 3e^- \quad (27)$$

Fe initially undergoes dissolution to form Fe^{2+}, which can complex with SO_4^{2-} to form $FeSO_4$(aq). As the applied potential increases to approximately −0.03 V, Fe-containing products are oxidized, resulting in the formation of $FePO_4$, Fe_2O_3, and FeO·OH. Additionally, once the applied potential exceeds 0.23 V, Fe^{2+} is further oxidized to Fe^{3+}, with a possible concomitant formation of $FeHPO_4^+$ in the electrolyte. Given that Fe is a primary composition of M42 HSS, these reactions are likely to occur (Lu and Chen, 2000; Hsiang et al., 2018; Yue et al., 2018; Mandal et al., 2020; Bai et al., 2021):

$$Fe \rightarrow Fe^{2+} + 2e^- \quad (28)$$

$$Fe^{2+} \rightarrow Fe^{3+} + e^- \quad (29)$$

$$Fe + SO_4^{2-} \rightarrow FeSO_4(aq) + 2e^- \quad (30)$$

$$Fe^{3+} + H_2PO_4^- \rightarrow FePO_4 + 2H^+ \quad (31)$$

$$FeSO_4(aq) + H_2PO_4^- \rightarrow FePO_4 + SO_4^{2-} + 2H^+ + e^- \quad (32)$$

$$2Fe^{2+} + 3H_2O \rightarrow Fe_2O_3 + 6H^+ + 2e^- \quad (33)$$

$$Fe^{2+} + 2H_2O \rightarrow FeO{\cdot}OH + 3H^+ + e^- \quad (34)$$

$$FePO_4 + 2H_2O \rightarrow FeO{\cdot}OH + H_2PO_4^- + H^+ \quad (35)$$

$$2FeO{\cdot}OH \rightarrow Fe_2O_3 + H_2O \quad (36)$$

$$Fe^{2+} + H_3PO_4(aq) \rightarrow FeHPO_4^+ + 2H^+ + e^- \quad (37)$$

It is evident that Mo initially undergoes oxidation to form MoO_2, but its thermodynamic stability region is relatively narrow. Once the applied potential exceeds 0.23 V, MoO_2 is further oxidized to MoO_3 and $HMoO_4^-$. Additionally, during the formation of Mo-containing products, other derivative reactions may occur, such as the oxidation of Mo^{3+} to MoO_2 (Yang et al., 1984; Winiarski et al., 2018; Shah et al., 2020).

$$Mo \rightarrow Mo^{3+} + 3e^- \quad (38)$$

$$Mo + 2H_2O \rightarrow MoO_2 + 4H^+ + 4e^- \quad (39)$$

$$Mo^{3+} + 2H_2O \rightarrow MoO_2 + 4H^+ + e^- \quad (40)$$

$$MoO_2 + 2H_2O \rightarrow HMoO_4^- + 3H^+ + 2e^- \quad (41)$$

$$MoO_2 + H_2O \rightarrow MoO_3 + 2H^+ + 2e^- \quad (42)$$

$$MoO_3 + H_2O \rightarrow HMoO_4^- + H^+ \quad (43)$$

Moreover, in the weak acidic environment, Mo-containing products may form MoO_2^{2+} and complex with SO_4^{2-} to form the compound MoO_2SO_4 (Alamdari and Sadrnezhaad, 2000; Cheema et al., 2018; Entezari-Zarandi et al., 2020). However, when the applied potential exceeds E_{TR}, indicating entry into the transpassive dissolution region, this compound cannot be detected in the corroded products, as shown in Fig. 10(d) and (f). Therefore, the formation of Mo-containing sulfate may occur in the applied potential range between E_{AP} and E_{TR}, as follows:

$$MoO_3 + H_2O \rightarrow H_2MoO_4(aq) \quad (44)$$

$$H_2MoO_4(aq) + 2H^+ \rightarrow MoO_2^{2+} + 2H_2O \quad (45)$$

$$MoO_2^{2+} + SO_4^{2-} \rightarrow MoO_2SO_4 \quad (46)$$

Furthermore, Co initially undergoes oxidative dissolution, appearing in the electrolyte as water-soluble Co^{2+} and $CoSO_4$ substances. However, as the applied potential increases to approximately 1.1 V, Co_3O_4 and CoO·OH begin to precipitate on the M42 HSS surface, gradually forming in the corroded products. Additionally, as the applied potential continues to increase, Co-containing products are ultimately oxidized to $Co(OH)_3$. Therefore, the corrosion process of Co involves an initial phase of oxidative dissolution, followed by passivation (Schubert et al., 2013; Lin et al., 2021; Zhang et al., 2023).

$$Co \rightarrow Co^{2+} + 2e^- \quad (47)$$

$$Co^{2+} \rightarrow Co^{3+} + e^- \quad (48)$$

$$Co + SO_4^{2-} \rightarrow CoSO_4(aq) + 2e^- \quad (49)$$

$$3Co^{2+} + 4H_2O \rightarrow Co_3O_4 + 8H^+ + 2e^- \quad (50)$$

$$Co^{2+} + 2H_2O \rightarrow CoO{\cdot}OH + 3H^+ + e^- \quad (51)$$

$$Co_3O_4 + 2H_2O \rightarrow 3CoO{\cdot}OH + H^+ + e^- \quad (52)$$

$$Co_3O_4 + 5H_2O \rightarrow 3Co(OH)_3 + H^+ + e^- \quad (53)$$

$$3CoSO_4(aq) + 4H_2O \rightarrow Co_3O_4 + 3SO_4^{2-} + 8H^+ + 2e^- \quad (54)$$

$$Co^{3+} + 3H_2O \rightarrow Co(OH)_3 + 3H^+ \quad (55)$$

It is noteworthy that the water-soluble sulfates described in Equations (23), (30), and (49) primarily exist in ionic states within the electrolyte (e.g., Cr^{2+}, Fe^{2+}, Co^{2+}, SO_4^{2-}) rather than as complexed forms with SO_4^{2-} (such as $CrSO_4(aq)$). These soluble compounds and ions primarily help explain the potential reaction mechanisms of these elements at the electrode–electrolyte interface. Moreover, the Pourbaix diagrams for the system mainly represent the most likely predominant species, without suggesting that metal ions such as Fe^{2+}/Fe^{3+}, Cr^{2+}/Cr^{3+}, and Co^{2+}/Co^{3+} are absent from the electrolyte or do not participate in reactions.

In summary, variations in applied potential significantly influence the formation of corroded products on the anodic surface. Additionally, alterations in applied potential are expected to affect the cathodic current on the Pt surface, potentially resulting in the electrodeposition of metal ions onto the Pt surface. The adsorption phenomenon on the cathodic surface requires a higher potential (such as 6 V), with the adsorbed products formed depending on the types of ions at the cathode-electrolyte interface. Based on the previous discussion, Fig. 15 presents the principal mechanisms driving product formation on the electrode surfaces in the M42 HSS-$H_2PO_4^-$-SO_4^{2-}–H_2O system. The product formation on the anodic and cathodic surfaces follows distinct mechanisms: the anodic surface is primarily driven by electrochemical reactions, whereas the cathodic surface mainly involves chemical reactions without electron participation, with the exception of hydrogen or oxygen reduction.

3.5.3. *Corrosion mechanism on the anodic surface of M42 HSS*

When the applied potential is below the potential E_{AP}, noticeable uniform corrosion along the grain boundaries is observed, as shown in Fig. 5(a). The various carbides formed during the heat treatment of M42 HSS lead to the depletion of alloying elements within the solid-solution strengthening phase, thereby increasing the alloy's susceptibility to corrosion (Alves et al., 2001). As reported by Vakili et al. (Vakili et al., 2015), carbides exhibit distinct corrosion potentials relative to the matrix, which can promote galvanic corrosion at the carbide-matrix interface. Moreover, Zhu et al. (Zhu et al., 2010) pointed out that the high free energy at the carbide-matrix interface and the diminished thermal stability of carbides result in more pronounced oxidation in carbide-rich regions compared to the surrounding matrix. The phase boundary between carbides and the matrix is theoretically regarded as a crystal defect, where substantial considerable energy is stored, leading to a more active interface (Zhao et al., 2018). Observations of corroded product layer's surfaces of M42 HSS show that severe corrosion primarily occurs in regions where carbides are concentrated in the matrix, potentially causing carbide detachment. This suggests that galvanic corrosion may occur at the carbide-matrix interface. Additionally, due to the strong affinity of carbides for oxygen under high oxygen partial pressure, they are prone to oxidation (Deng et al., 2019), supporting the observed carbide oxidation in the electrochemical process (see Fig. 5 and Table 2).

As the applied potential increases, corrosion along the grain

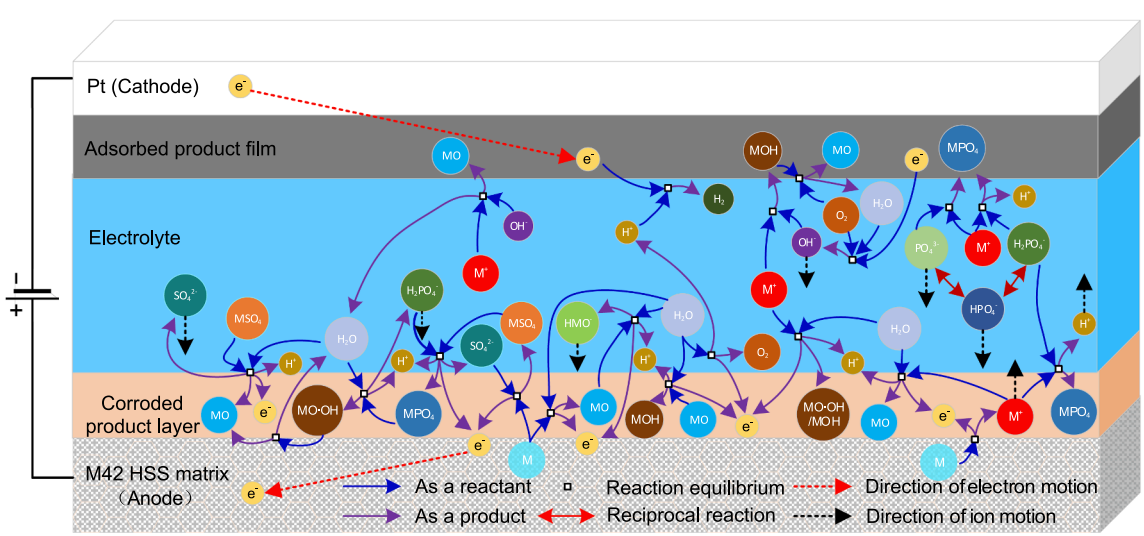

Fig. 15. Schematic diagram of principal mechanisms for product formation between electrodes in the M42 HSS-$H_2PO_4^-$-SO_4^{2-}–H_2O system. M, M^+, MO, MOH (or MO·OH), HMO^-, MSO_4, and MPO_4 represent the metal atom, metal ion, metal oxide, metal (or oxide) hydrate, acidic metal oxyanions, metal sulfate, and metal phosphate, respectively.

boundaries becomes exposed more apparent, as shown in Fig. 5(c), initiating the formation and propagation of microcracks on the surface of corroded product layer (Yin et al., 2020). Once the applied potential exceeds the potential E_{TR}, corroded products progressively detach due to bubble-induced disturbances and internal stress enhancement. This process may cause localized dissolution of the corroded products, leading to the formation of small pits on the corroded surface, giving it a honeycomb-like appearance. High-energy phase boundaries, with their high defect density, are more likely to breakdown, showing increased sensitivity to pitting nucleation (Seyeux et al., 2009). According to the local corrosion mechanism proposed by Marcus et al. (Marcus et al., 2008), SO_4^{2-}, PO_4^{3-}, and OH^- compete for adsorption at phase boundary sites, with preferential adsorption and complex formation occurring. However, based on the XPS analysis results of the surface of corroded product layer of M42 HSS (see Fig. 10), it is suggested that SO_4^{2-} and OH^- complexes have weaker binding to the matrix, thereby reducing ionization activation energy. This leads to increased local corrosion dissolution and diminishes the formation of the corroded products. Besides carbide detachment, localized corrosion and pitting may also occur on the corroded surface. Nevertheless, as H^+ is gradually consumed, the localized increase in pH in the electrolyte promotes the re-passivation of the alloy, enhancing resistance to pitting (Baba et al., 2002). Therefore, during the electrochemical corrosion process, the corroded surface of the anode may exhibit one or more corrosion mechanisms, depending on the specific conditions. However, as some studies have noted (Ma et al., 2023; Wang et al., 2023a), electrochemical corrosion machining for metals and their alloys might not attain an optimal surface quality. To improve the surface quality for repairing HSS roll surfaces, modifications to the electrolyte flow state (non-stagnant), workpiece movement (e.g., rotation), and processing parameters (e.g., applied potential) may be required. Moreover, combining electrochemical corrosion machining with grinding (Wang et al., 2023a) or implementing grinding after electrochemical corrosion machining (Ma et al., 2023) could be used to enhance the surface quality, among other possible approaches.

4. Conclusions

M42 HSS is a premium alloy extensively used in the manufacturing of rolls in the steel rolling industry. This study systematically investigates the electrochemical corrosion process and behavior for M42 HSS in the $H_2PO_4^-$-SO_4^{2-} passivating electrolyte, with a focus on elucidating the intricate corrosion phenomena, varying processes, and underlying mechanisms of product formation and corrosion in the M42 HSS-$H_2PO_4^-$-SO_4^{2-}–H_2O system. The following significant conclusions can be drawn from this study:

(1) The microstructure of M42 HSS comprises a tempered martensitic matrix with two types of eutectic carbides. Mo-rich M_2C carbides tend to aggregate along grain boundaries, while Fe- and Mo-rich M_6C carbides are uniformly distributed throughout the matrix.
(2) In the $H_2PO_4^-$-SO_4^{2-} passivating electrolyte, M42 HSS exclusively shows characteristics of oxidative reactions. A Pourbaix diagram for the M42 HSS-$H_2PO_4^-$-SO_4^{2-}–H_2O system exhibits regions of immunity, corrosion, passivation, and possible passivation/corrosion, with variations in applied potential leading to changes in dominant species. These changes are supported by XPS, XRD, and ICP analysis results.
(3) Electrochemical corrosion of HSS primarily results in uniform corrosion along grain boundaries, accompanied by concurrent carbide oxidation. Selective corrosion may occur in the matrix. The enhanced reactivity at the carbide-matrix interface significantly contributes to carbide detachment, with potentials exceeding E_{TR} leading to pitting.
(4) Corroded products on M42 HSS surfaces mainly comprise carbides, oxides, hydroxides, and phosphates. Thermodynamic properties and elemental distribution variations across the corroded product layer surface are discernible. Higher applied potential dissolves specific products, contributing to localized porosity, pits, or small dimples on the corroded surface.
(5) On the cathodic surface, cations such as Fe^{2+}/Fe^{3+} react with surrounding anions like OH^- and PO_4^{3-}, leading to the formation of adsorbed products at the cathode. The cathode itself shows no evidence of degradation or loss. The insoluble products primarily consist of corroded products that have detached from the anodic surface, along with minimal flocculent precipitates formed within the electrolyte.
(6) Variations in applied potential significantly influence the formation of corroded products on the anodic surface, while the adsorption phenomenon on the cathodic surface requires a higher potential (such as 6 V) to occur. The adsorbed products depend on the ion species. The mechanisms of product formation on the anodic and cathodic surfaces are distinct: the anodic surface is primarily driven by electrochemical reactions, whereas the cathodic surface mainly involves chemical reactions without electron participation, with the exception of hydrogen or oxygen reduction.

Furthermore, in this study, Pt was used as the cathode, but its application in actual electrochemical corrosion machining or ECG processes is unlikely due to its high cost. In our previous studies (Cao et al., 2022; Yuan et al., 2022), the 1Cr18Ni9Ti cathodic tool showed a noticeable black product film on its surface during the medium-pole-based ECG process. Therefore, investigating the deposits on the Pt electrode surface provides valuable insights into practical electrochemical corrosion machining applications. In practical electrochemical corrosion machining applications, the electrolyte is typically in a flowing state. However, in this study, the electrolyte was static, potentially resulting in variations in the elemental distribution of corroded products, affecting their uniformity. Future research will focus on the corrosion behavior of HSS during practical electrochemical corrosion machining processes to understand these mechanisms better and address practical challenges.

CRediT authorship contribution statement

Gang Cao: Writing – review & editing, Writing – original draft, Validation, Methodology, Investigation, Formal analysis, Data curation, Conceptualization. **Huaichao Wu:** Validation, Supervision, Resources, Project administration, Funding acquisition, Conceptualization. **Guangqin Wang:** Writing – review & editing, Methodology, Formal analysis, Data curation. **Long Nie:** Validation, Methodology, Investigation. **Kui Yuan:** Writing – review & editing, Validation, Supervision. **Bin Ji:** Methodology, Formal analysis, Data curation.

Declaration of Competing Interest

The authors declare that they have no known competing financial interests or personal relationships that could have appeared to influence the work reported in this paper.

Acknowledgements

This work was supported by the Key Laboratory Project of Guizhou Higher Education Institutions (Grant No. Q. J. J [2023] 009); the Major Science and Technology Project in Guizhou Province (Grant No. Q. K. H. Z. D. Z. X. Z [2019] 3016); and the Cultivation Project in Guizhou University (Grant No. G. D. P. Y [2019] 02).

Appendix A. Supplementary data

Supplementary data to this article can be found online at https://doi.org/10.1016/j.arabjc.2024.105940.

References

Alamdari, E.K., Sadrnezhaad, S.K., 2000. Thermodynamics of extraction of MoO_4^{2-} from aqueous sulfuric acid media with TBP dissolved in kerosene. Hydrometallurgy 55, 327–341.

Alves, V.A., Brett, C.M.A., Cavaleiro, A., 2001. Influence of heat treatment on the corrosion of high speed steel. J. Appl. Electrochem. 31, 65–72.

Anwar, M., Alghamdi, K.S., Zulfiqar, S., Warsi, M.F., Waqas, M., Hasan, M., 2023. Ag-decorated BiOCl anchored onto the g-C_3N_4 sheets for boosted photocatalytic and antimicrobial activities. Opt. Mater. 135, 113336.

Baba, H., Kodama, T., Katada, Y., 2002. Role of nitrogen on the corrosion behavior of austenitic stainless steels. Corros. Sci. 44, 2393–2407.

Bai, B., Xiao, G., Deng, L., Zhang, N., Chen, C., Bu, Y., Che, D., 2021. A study on corrosion behavior of 15CrMo in saturated saline steam with sodium sulfate. Corros. Sci. 181, 109240.

Banu, A., Marcu, M., Juganaru, C., Osiceanu, P., Anastasescu, M., Capra, L., 2019. Corrosion behavior of CoCrMoW cast alloy in lactic acid environment for surgical applications. Arab. J. Chem. 12, 2007–2016.

Barchiche, C., Deslouis, C., Festy, D., Gil, O., Refait, P., Touzain, S., Tribollet, B., 2003. Characterization of calcareous deposits in artificial seawater by impedance techniques: 3-Deposit of $CaCO_3$ in the presence of Mg (II). Electrochim. Acta 48, 1645–1654.

Barchiche, C., Sabot, R., Jeannin, M., Refait, P., 2010. Corrosion of carbon steel in sodium methanoate solutions. Electrochim. Acta 55, 1940–1947.

Benabdellah, M., Tounsi, A., Khaled, K.F., Hammouti, B., 2011. Thermodynamic, chemical and electrochemical investigations of 2-mercapto benzimidazole as corrosion inhibitor for mild steel in hydrochloric acid solutions. Arab. J. Chem. 4, 17–24.

Biesinger, M.C., Payne, B.P., Grosvenor, A.P., Lau, L.W., Gerson, A.R., Smart, R.S.C., 2011. Resolving surface chemical states in XPS analysis of first row transition metals, oxides and hydroxides: Cr, Mn, Fe, Co and Ni. Appl. Surf. Sci. 257, 2717–2730.

Bonola, B., Sosa-Rodríguez, F., Lara, R.H., García-Solares, S.M., Mena-Cervantes, V.Y., Lartundo-Rojas, L., Vazquez-Arenas, J., Hernández-Altamirano, R., 2022. Sustainable and fast elimination of high Cr (III) concentrations from real tannery wastewater using an electrochemical-chemical process forming Cr_2FeO_4. Sep. Purif. Technol. 294, 121211.

Bratsch, S.G., 1989. Standard electrode potentials and temperature coefficients in water at 298.15 K. J. Phys. Chem. Ref. Data 18, 1–21.

Brett, C.M.A., Melo, P.I.C., 1997. Influence of anions on the corrosion of high speed steel. J. Appl. Electrochem. 27, 959–964.

Cao, G., Wu, H., Wang, G., Nie, L., Yuan, K., 2022. Selection of a suitable electrolyte for electrochemical grinding of high-speed steel roll material based on electrochemical techniques and uniform design machining experiments. Int. J. Adv. Manuf. Tech. 122, 3129–3147.

Cetiner, Z.S., Wood, S.A., Gammons, C.H., 2005. The aqueous geochemistry of the rare earth elements. Part XIV. The solubility of rare earth element phosphates from 23 to 150 °C. Chem. Geol. 217, 147–169.

Chaus, A.S., Bračík, M., Sahul, M., Dománková, M., 2019. Microstructure and properties of M2 high-speed steel cast by the gravity and vacuum investment casting. Vacuum 162, 183–198.

Chaus, A.S., Sahul, M., Moravčík, R., Sobota, R., 2021. Role of microstructural factor in wear resistance and cutting performance of high-speed steel end mills. Wear 474, 203865.

Cheema, H.A., Ilyas, S., Masud, S., Muhsan, M.A., Mahmood, I., Lee, J.C., 2018. Selective recovery of rhenium from molybdenite flue-dust leach liquor using solvent extraction with TBP. Sep. Purif. Technol. 191, 116–121.

Chen, D., Liu, M., Liu, X., Zhou, Y., Wang, X., Zhou, Y., 2021. Oxidation behavior of 304 stainless steel with modified layer by plasma nitriding in High temperature and pressurized Water. Corros. Sci. 186, 109468.

Criss, C.M., Cobble, J.W., 1964. The thermodynamic properties of high temperature aqueous solutions. IV. Entropies of the ions up to 200° and the correspondence principle. J. Am. Chem. Soc. 86, 5385–5390.

Dang, J., Zhang, G.H., Chou, K.C., 2014. Phase transitions and morphology evolutions during hydrogen reduction of MoO_3 to MoO_2. High Temp. Mat. Pr-Isr. 33, 305–312.

Delaunois, F., Stanciu, V.I., Megret, A., Sinnaeve, M., 2022. Oxidation and wear behavior of high-speed steel and semi-high-speed steel used in hot strip mill. Int. J. Adv. Manuf. Tech. 119, 677–689.

Deng, G.Y., Tieu, A.K., Su, L.H., Zhu, H.T., Reid, M., Zhu, Q., Kong, C., 2019. Microstructural study and residual stress measurement of a hot rolling work roll material during isothermal oxidation. Int. J. Adv. Manuf. Tech. 102, 2107–2118.

El-Naggar, M.M., 2006. Effects of Cl^-, NO_3^- and SO_4^{2-} anions on the anodic behavior of carbon steel in deaerated 0.50 M $NaHCO_3$ solutions. Appl. Surf. Sci. 252, 6179–6194.

Entezari-Zarandi, A., Azizi, D., Nikolaychuk, P.A., Larachi, F., Pasquier, L.C., 2020. Selective recovery of molybdenum over rhenium from molybdenite flue dust leaching solution using PC88A extractant. Metals 10, 1423.

Figlarz, M., Guenot, J., Tournemolle, J.N., 1974. Oxidation of cobalt (II) hydroxide to oxide hydroxide: solids evolution during reaction. J. Mater. Sci. 9, 772–776.

Fredriksson, W., Malmgren, S., Gustafsson, T., Gorgoi, M., Edström, K., 2012. Full depth profile of passive films on 316L stainless steel based on high resolution HAXPES in combination with ARXPS. Appl. Surf. Sci. 258, 5790–5797.

Garza-Montes-de-Oca, N.F., Rainforth, W.M., 2009. Wear mechanisms experienced by a work roll grade high speed steel under different environmental conditions. Wear 267, 441–448.

Ge, Y., Zhu, Z., Wang, D., 2017. Electrochemical dissolution behavior of the nickel-based cast superalloy K423A in $NaNO_3$ solution. Electrochim. Acta 253, 379–389.

Ghali, E., 2010. Corrosion resistance of aluminum and magnesium alloys: understanding, performance, and testing. John Wiley & Sons, New York.

Gossenberger, F., Juarez, F., Groß, A., 2020. Sulfate, bisulfate, and hydrogen co-adsorption on Pt (111) and Au (111) in an electrochemical environment. Front. Chem. 8, 634.

Grinon-Echaniz, R., Refait, P., Jeannin, M., Sabot, R., Paul, S., Thornton, R., 2021. Study of cathodic reactions in defects of thermal spray aluminium coatings on steel in artificial seawater. Corros. Sci. 187, 109514.

Guo, C., Shi, S., Dai, H., Yu, J., Chen, X., 2022. Corrosion mechanisms of nickel-based alloys in chloride-containing hydrofluoric acid solution. Eng. Fail. Anal. 140, 106580.

Han, L., Li, J., Fei, X., Wang, M., Liu, S., Zhang, X., Xue, Q., 2023. Stabilization and strengthening of chromium (VI)-contaminated soil via magnesium ascorbyl phosphate (MAP) and phytase addition. J. Hazard. Mater. 448, 130860.

Han, H., Sun, W., Hu, Y., Cao, X., Tang, H., Liu, R., Yue, T., 2016. Magnetite precipitation for iron removal from nickel-rich solutions in hydrometallurgy process. Hydrometallurgy 165, 318–322.

Hsiang, H.I., Fan, L.F., Hung, J.J., 2018. Phosphoric acid addition effect on the microstructure and magnetic properties of iron-based soft magnetic composites. J. Magn. Magn. Mater. 447, 1–8.

Huang, S., Wang, J., Wei, X., Zhou, Y., Wang, L., Zhang, J., 2019. Microstructural characterization and film-forming mechanism of a phosphate chemical conversion ceramic coating prepared on the surface of 2A12 aluminum alloy. Rsc Adv. 9, 18767–18775.

Jiao, W.C., Li, H.B., Feng, H., Jiang, Z.H., Wang, H.J., Zhu, H.C., Han, P.D., Wu, W., 2022a. Significant improvement of cleanliness and macro/microstructure of as-cast AISI M42 high-speed steel by Mg treatment. Metall. Mater. Trans. B 53, 1196–1211.

Jiao, W.C., Li, H.B., Feng, H., Wang, H.J., Jiang, Z.H., Wu, W., 2022b. High-temperature annealing significantly enhances intrinsic hot workability of the as-cast high-nitrogen M42 high-speed steel. Metall. Mater. Trans. B A 53, 2426–2451.

Jing, Q., Zhang, J., Liu, Y., Yang, C., Ma, B., Chen, Y., Wang, C., 2019. E-pH diagrams for the Li-Fe-P-H_2O system from 298 to 473 K: thermodynamic analysis and application to the wet chemical processes of the $LiFePO_4$ cathode material. J. Phys. Chem. C 123, 14207–14215.

Jovičević-Klug, P., Jenko, M., Jovičević-Klug, M., Batič, B.Š., Kovač, J., Podgornik, B., 2021. Effect of deep cryogenic treatment on surface chemistry and microstructure of selected high-speed steels. Appl. Surf. Sci. 548, 149257.

Klocke, F., Herrig, T., Zeis, M., Klink, A., 2018. Comparison of the electrochemical machinability of electron beam melted and casted gamma titanium aluminide TNB-V5. P. i. Mech. Eng. B-J. Eng. 232, 586–592.

Kwok, C.T., Cheng, F.T., Man, H.C., 2007. Microstructure and corrosion behavior of laser surface-melted high-speed steels. Surf. Coat. Tech. 202, 336–348.

Lin, S., Niu, L., Pan, X., Liang, Z., Zhang, T., 2021. Study on preparation and recovery of cobalt hydroxide and cobalt carbonate. Hydrometallurgy 203, 105518.

Liu, Z., Fu, P., Zhao, J., Ji, F., Zhang, Y., Nagaumi, H., Wang, X., Zhao, Y., Jia, P., Li, W., 2020b. Corrosion and high-temperature tribological behavior of carbon steel claddings by additive manufacturing technology. Surf. Coat. Tech. 384, 125325.

Liu, X., Wu, X., Han, E.H., 2011. Influence of Zn injection on characteristics of oxide film on 304 stainless steel in borated and lithiated high temperature water. Corros. Sci. 53, 3337–3345.

Liu, X., Li, Q., Zhang, Y., Jiang, T., Yang, Y., Xu, B., He, Y., 2020a. Electrochemical behaviour of the dissolution and passivation of arsenopyrite in 9K culture medium. Appl. Surf. Sci. 508, 145269.

Liu, M., Zeng, Y., Luo, J.L., 2023. Roles of major alloying elements in steels and alloys on corrosion under biomass hydrothermal liquefaction (HTL) conversion. Corros. Sci. 218, 111148.

Lohrengel, M.M., Klüppel, I., Rosenkranz, C., Bettermann, H., Schultze, J.W., 2003. Microscopic investigations of electrochemical machining of Fe in $NaNO_3$. Electrochim. Acta 48, 3203–3211.

Lu, Z.P., Chen, J.M., 2000. Magnetic field effects on anodic polarisation behaviour of iron in neutral aqueous solutions. Corros. Eng. Sci. Techn. 35, 224–228.

Lyu, L., Wang, F., Qiao, J., Ding, X., Zhang, X., Xu, D., Liu, W., Liu, J., 2020. Novel synthesis of $MoO_3/Mo_4O_{11}/MoO_2$ heterogeneous nanobelts for wideband electromagnetic wave absorption. J. Alloy. Compd. 817, 153309.

Ma, X., Jiao, F., Niu, Y., Wang, X., Hu, Z., Bie, W., Yang, G., 2023. Modeling of the material removal rate in internal cylindrical plunge electrochemical grinding. J. Manuf. Process 92, 89–106.

Ma, H., Wang, W., Liu, Y., Liu, X., He, A., Dong, Y., Wang, Y., Li, J., 2024. Nitrogen-induced optimization of corrosion resistance for nanocrystalline soft magnetic Fe-Zr-B alloys. J. Mater. Sci. Technol. 186, 15–27.

Macdonald, D.D., Scott, A.C., Wentrcek, P., 1979. External reference electrodes for use in high temperature aqueous systems. J. Electrochem. Soc. 126, 908.

Mandal, S., Singh, J.K., Lee, D.E., Park, T., 2020. Ammonium phosphate as inhibitor to mitigate the corrosion of steel rebar in chloride contaminated concrete pore solution. Molecules 25, 3785.

Marcus, P., Maurice, V., Strehblow, H.H., 2008. Localized corrosion (pitting): A model of passivity breakdown including the role of the oxide layer nanostructure. Corros. Sci. 50, 2698–2704.

Marcus, P., Protopopoff, E., 1997. Potential-pH diagrams for sulfur and oxygen adsorbed on chromium in water. J. Electrochem. Soc. 144, 1586.

Munawar, T., Nadeem, M.S., Mukhtar, F., Manzoor, S., Ashiq, M.N., Batool, S., Hasan, M., Iqbal, F., 2023. Multifunctional dual Z-scheme heterostructured Sm_2O_3-WO_3-La_2O_3 nanocomposite: Enhanced electrochemical, photocatalytic, and antibacterial properties. Adv. Powder Technol. 34, 104061.

[dataset] Naumkin, A.V., Kraut-Vass, A., Gaarenstroom, S.W., Powell, C.J., 2023. NIST X-ray Photoelectron Spectroscopy Database, v5. https://dx.doi.org/10.18434/T4T88K.
Qu, H., Liao, B., Liu, L., Li, D., Guo, J., Ren, X., Yang, Q., 2012. Precipitation rule of carbides in a new high speed steel for rollers. Calphad 36, 144–150.
Ripoll, M.R., Ojala, N., Katsich, C., Totolin, V., Tomastik, C., Hradil, K., 2016. The role of niobium in improving toughness and corrosion resistance of high speed steel laser hardfacings. Mater. Design 99, 509–520.
Rosas-Becerra, G., Mejía-Caballero, I., Martínez-Trinidad, J., Palomar-Pardavé, M., Romero-Romo, M., Pérez-Pasten-Borja, R., Campos-Silva, I., 2017. Electrochemical corrosion behavior of borided CoCrMo alloy immersed in hanks' solution. J. Mater. Eng. Perform. 26, 704–714.
Roy, S., Zebardast, H., Asselin, E., 2012. On the development of thermo-kinetic Eh-pH diagrams. Metall. Mater. Trans. B 43, 1277–1283.
Sahoo, G., Balasubramaniam, R., 2008. On the corrosion behavior of phosphoric irons in simulated concrete pore solution. Corros. Sci. 50, 131–143.
Schmickler, W., Santos, E., 2010. Interfacial electrochemistry. Springer, Berlin.
Schubert, N., Schneider, M., Michealis, A., 2013. The mechanism of anodic dissolution of cobalt in neutral and alkaline electrolyte at high current density. Electrochim. Acta 113, 748–754.
Schulmeyer, W.V., Ortner, H.M., 2002. Mechanisms of the hydrogen reduction of molybdenum oxides. Int. J. Refract. Met. h. 20, 261–269.
Serna, M.M., Rossi, J.L., 2009. MC complex carbide in AISI M2 high-speed steel. Mater. Lett. 63, 691–693.
Seyeux, A., Maurice, V., Marcus, P., 2009. Breakdown kinetics at nanostructure defects of passive films. Electrochem. Solid St. 12, C25.
Shah, M., Ayob, M.T.M., Rosdan, R., Yaakob, N., Embong, Z., Othman, N.K., 2020. The effect of H_2S pressure on the formation of multiple corrosion products on 316L stainless steel surface. Sci. World J. 2020, 3989563.
Shi, S.C., Su, C.C., 2016. Corrosion inhibition of high speed steel by biopolymer HPMC derivatives. Materials 9, 612.
Subramanyam, V., Kumar, J., Singh, S.N., 2022. Temporal synchronization framework of machine-vision cameras for high-speed steel surface inspection systems. J. Real-Time Image Pr. 19, 445–461.
Tardio, S., Abel, M.L., Carr, R.H., Castle, J.E., Watts, J.F., 2015. Comparative study of the native oxide on 316L stainless steel by XPS and ToF-SIMS. J. Vac. Sci. Technol. A 33.
Vakili, S., Akbari, A., Mohammadzadeh, R., 2015. Corrosion resistance of plasma nitrided AISI M2 high speed steel. Prot. Met. Phys. Chem+ 51, 630–636.
Vieillard, P., Tardy, Y., 1984. Thermochemical properties of phosphates. Springer, Berlin.
Voglar, J., Novak, Ž., Jovičević-Klug, P., Podgornik, B., Kosec, T., 2020. Effect of deep cryogenic treatment on corrosion properties of various high-speed steels. Metals 11, 14.
Wang, K., Han, J., Gerard, A.Y., Scully, J.R., Zhou, B.C., 2020. Potential-pH diagrams considering complex oxide solution phases for understanding aqueous corrosion of multi-principal element alloys. Npj Mat. Degrad. 4, 35.
Wang, T., Liu, Y., Wang, K., Lv, Z., 2023a. Investigation on a sustainable composite method of glass microstructures fabrication-Electrochemical discharge milling and grinding (ECDM-G). J. Clean. Prod. 387, 135788.
Wang, Y., Xu, Z., Zhang, A., 2019. Electrochemical dissolution behavior of Ti-45Al-2Mn-2Nb + 0.8 vol% TiB2 XD alloy in NaCl and $NaNO_3$ solutions. Corros. Sci. 157, 357–369.
Wang, Y., Wang, B., He, S., Zhang, L., Xing, X., Li, H., Lu, M., 2022a. Unraveling the effect of H_2S on the corrosion behavior of high strength sulfur-resistant steel in CO_2/H_2S/Cl^- environments at ultra high temperature and high pressure. J. Nat. Gas Sci. Eng. 100, 104477.
Wang, Y., Wang, B., Xing, X., He, S., Zhang, L., Lu, M., 2022b. Effects of flow velocity on the corrosion behaviour of super 13Cr stainless steel in ultra-HTHP CO_2-H_2S coexistence environment. Corros. Sci. 200, 110235.
Wang, Y., Mao, B., Chu, S., Chen, S., Xing, H., Zhao, H., Wang, S., Wang, Y., Zhang, J., Sun, B., 2023b. Advanced manufacturing of high-speed steels: A critical review of the process design, microstructural evolution, and engineering performance. J. Mater. Res. Technol. 24, 8198–8240.
Wang, J., Zhang, Z., Xue, W., Zhu, H., Xu, K., Liu, Y., 2024. Electrochemical dissolution behavior of 07Cr16Ni6 alloy in sodium nitrate solution. Arab. J, Chem, p. 105708.
Winiarski, J., Tylus, W., Lutz, A., De Graeve, I., Szczygieł, B., 2018. The study on the corrosion mechanism of protective ternary ZnFeMo alloy coatings deposited on carbon steel in 0.5 mol/dm^{-3}(−|-) NaCl solution. Corros. Sci. 138, 130–141.
Wongpanya, P., Siritapetawee, J., Wongpinij, T., Photongkam, P., 2022. Effect of antiplatelet drugs on corrosion of 316L stainless steel for application to biomaterials. Mater. Chem. Phys. 278, 125596.
Xia, D.H., Luo, J.L., 2019. Effects of reduced sulfur on passive film properties of steam generator (SG) tubing: an overview. Anti-Corros. Method. m. 66, 317–326.
Xu, L., Song, W., Ma, S., Zhou, Y., Pan, K., Wei, S., 2021. Effect of slippage rate on frictional wear behaviors of high-speed steel with dual-scale tungsten carbides (M_6C) under high-pressure sliding-rolling condition. Tribol. Int. 154, 106719.
Xu, L.J., Zhang, S.M., Wei, S.Z., 2011. Modeling Corrosion Property of High Vanadium High Speed Steel (HVHSS) under H_3PO_4 Medium Condition Using Artificial Neural Network. Adv. Mech. Eng. 52, 1243–1246.
Yang, X., Huang, X., Qiu, T., Jiao, X., 2016. Application of Eh-pH Diagram for Activation of Depressed Chalcopyrite in Cyanidation Tailings. Min. Proc. Ext. Met. Rev. 37, 134–138.
Yang, J., Liu, H., Martens, W.N., Frost, R.L., 2010. Synthesis and characterization of cobalt hydroxide, cobalt oxyhydroxide, and cobalt oxide nanodiscs. J. Phys. Chem. C 114, 111–119.
Yang, W., Ni, R.C., Hua, H.Z., Pourbaix, A., 1984. The behavior of chromium and molybdenum in the propagation process of localized corrosion of steels. Corros. Sci. 24, 691–707.
Yao, J., Ding, Y., Liu, R., Zhang, Q., Wang, L., 2018. Wear and corrosion performance of laser-clad low-carbon high-molybdenum Stellite alloys. Opt. Laser Technol. 107, 32–45.
Yin, Y., Zhang, J., Ma, Y., Huo, J., Zhao, K., Meng, X., Han, Q., Yin, J., 2020. Electrochemical dissolution behavior of nickel-based Hastelloy X superalloy at low current densities. Ieee Access 8, 62714–62724.
Yuan, K., Wu, H., Yang, L., Zhao, L., Wang, Y., He, M., 2020. Experiments, analysis and parametric optimization of roll grinding for high-speed steel W6Mo5Cr4V2. Int. J. Adv. Manuf. Tech. 109, 1275–1284.
Yuan, K., Wu, H., Cao, G., Nie, L., Ji, B., 2022. Design and optimization of cathode for ECM of high-speed steel roll material based on multi-physics field coupling analysis. Int. J. Adv. Manuf. Tech. 121, 7983–7995.
Yue, Y., Liu, C., Shi, P., Jiang, M., 2018. Passivity of stainless steel in sulphuric acid under chemical oxidation. Corros. Eng. Sci. Techn. 53, 173–182.
Zeng, W.M., Peng, Y.P., Peng, T.J., Nan, M.H., Chen, M., Qiu, G.Z., Shen, L., 2020. Electrochemical studies on dissolution and passivation behavior of low temperature bioleaching of chalcopyrite by Acidithiobacillus ferrivorans YL15. Miner. Eng. 155, 106416.
Zhang, X., Feng, C., Dong, B., Liu, C., Chai, Y., 2023. High-Voltage-Enabled Stable Cobalt Species Deposition on MnO_2 for Water Oxidation in Acid. Adv. Mater. 35, 2207066.
Zhao, Y., Li, X., Zhang, C., Zhang, T., Xie, J., Zeng, G., Xu, D., Wang, F., 2018. Investigation of the rotation speed on corrosion behavior of HP-13Cr stainless steel in the extremely aggressive oilfield environment by using the rotating cage test. Corros. Sci. 145, 307–319.
Zhao, Y., Xie, J., Zeng, G., Zhang, T., Xu, D., Wang, F., 2019. Pourbaix diagram for HP-13Cr stainless steel in the aggressive oilfield environment characterized by high temperature, high CO_2 partial pressure and high salinity. Electrochim. Acta 293, 116–127.
Zhengyang, X.U., Yudi, W.A.N.G., 2021. Electrochemical machining of complex components of aero-engines: Developments, trends, and technological advances. Chinese J. Aeronaut. 34, 28–53.
Zhou, X., Liao, C., Wang, Y., Zhu, Y., 2021. Constructing the Pourbaix diagram of Fe-Cl–H2O ternary system under supercritical water conditions. Electrochim. Acta 377, 138075.
Zhu, Q., Zhu, H.T., Tieu, A.K., Reid, M., Zhang, L.C., 2010. In-situ investigation of oxidation behaviour in high-speed steel roll material under dry and humid atmospheres. Corros. Sci. 52, 2707–2715.